JOURNAL OF GEOPHYSICAL RESEARCH, VOL. 103, NO. D4, PAGES 3825-3846, FEBRUARY 27, 1998

Measurements of the downward longwave radiation spectrum over the Antarctic Plateau and comparisons with a line-by-line radiative transfer model for clear skies

Von P. Walden

Space Science and Engineering Center, University of Wisconsin, Madison

Stephen G. Warren

Department of Atmospheric Sciences, University of Washington, Seattle

Frank J. Murcray

Department of Physics, University of Denver, Denver, Colorado

Abstract. A 1-year field program was conducted at South Pole Station in 1992 to measure the downward infrared radiance spectrum at a resolution of 1 cm^{-1} over the spectral range 550-1667 cm^{-1}. The atmosphere over the Antarctic Plateau is the coldest and driest on Earth, where in winter, surface temperatures average about -60°C, the total column water vapor is as low as 300 μm of precipitable water, and the clear-sky downward longwave flux is usually less than 80 W m^{-2}. Three clear-sky test cases are selected, one each for summer, winter, and spring, for which high-quality radiance data are available as well as ancillary data to construct model atmospheres from radiosondes, ozonesondes, and other measurements. The model atmospheres are used in conjunction with the line-by-line radiative transfer model (LBLRTM) to compare model calculations with the spectral radiance measurements. The high-resolution calculations of LBLRTM (≈0.001 cm^{-1}) are matched to the lower-resolution measurements (1 cm^{-1}) by adjusting their spectral resolution and by applying a correction for the finite field of view of the interferometer. In summer the uncertainties in temperature and water vapor profiles dominate the radiance error in the LBLRTM calculations. In winter the uncertainty in viewing zenith angle becomes important as well as the choice of atmospheric levels in the strong near-surface temperature inversion. The spectral radiance calculated for each of the three test cases generally agrees with that measured, to within twice the total estimated radiance error, thus validating LBLRTM to this level of accuracy for Antarctic conditions. However, the discrepancy exceeds twice the estimated error in the gaps between spectral lines in the region 1250-1500 cm^{-1}, where emission is dominated by the foreign-broadened water vapor continuum.

1. Introduction

The Antarctic Plateau covers large areas of East Antarctica (above 2000 m) and West Antarctica (above 1500 m). In its longwave radiation budget this region differs from the katabatic wind region [*Yamanouchi and Kawaguchi*, 1984, 1985] and the maritime Antarctic [*Lubin*, 1994]. For most of the year a near-surface temperature inversion is present over the plateau, whose strength increases with surface elevation as the atmosphere becomes thinner and less absorptive to infrared radiation. Large radiation losses to space occur throughout most of the year, with frontal activity and the associated cloudiness temporarily reducing the loss at the surface [e.g., *Stone et al.*, 1989; *Stone and Kahl*, 1991].

Continuous records of meteorological data from the East Antarctic Plateau exist for three stations: 40 years at South Pole (90°S), 40 years at Vostok (78°S, 107°E), and 3 years at Plateau (79°S, 40°E). Since there is little regional variation in climate across the plateau, data from one location can represent a large geographical area. Thus, in the absence of data at other locations, atmospheric conditions at South Pole Station may serve to represent the conditions over most of East Antarctica. Recent attempts to model the climate of the Antarctic have met with some success in comparing model output with existing observational data sets [*Tzeng et al.*, 1993, 1994; *Genthon*, 1994]. For the purpose of this paper the most important characteristic of the atmosphere over the Antarctic interior is that it is the coldest and driest on Earth and thus represents an endpoint of terrestrial climate.

In the 1980s a project on Intercomparison of Radiation Codes used in Climate Models (ICRCCM) was established to compare radiative transfer models, ranging from detailed line-by-line codes to highly parameterized band models [*Luther et al.*, 1988; *Ellingson and Fouquart*, 1991]. The results of clear-sky calculations for shortwave models were summarized by *Fouquart et al.* [1991] and those for longwave models by *Ellingson et al.* [1991]. The atmospheres used in those comparisons were the five reference atmospheres of the Air Force Geophysics Laboratory (AFGL) [*McClatchey et al.*, 1972] as well as isothermal atmospheres containing only CO_2 or H_2O as gaseous absorbers. One of the main

Paper number 97JD02433.
0148-0227/98/97JD-02433$09.00

conclusions of the longwave study was that line-by-line radiative transfer models, although they agree well with each other, do not represent an absolute standard by which to judge less detailed models. Their output must therefore be compared with data from the real atmosphere. Spectral rather than broadband, and radiance rather than flux measurements, would be most useful because the causes of discrepancies between model and observation can be more easily identified if angular and spectral averaging has not been done. Specifically, the study concluded that spectral radiance data of moderate resolution (about 1 cm^{-1}) would be particularly valuable for comparison with a variety of radiation codes at various spectral resolutions.

To resolve the differences among the most detailed radiation models, the ICRCCM participants recommended that accurate spectral radiance measurements be made coincidentally with the atmospheric variables necessary to calculate radiance [*Ellingson et al.*, 1991]. Currently, data sets of this type exist for the following locations: (1) Coffeyville, Kansas, where the Spectral Radiance Experiment (SPECTRE) was performed [*Ellingson and Wiscombe*, 1996], (2) the Southern Great Plains site of the Atmospheric Radiation Measurement (ARM) program [*Stokes and Schwartz*, 1994; *Ellingson et al.*, 1995], (3) the California coast [*Clough et al.*, 1989a], and (4) the tropical Pacific Ocean [*Lubin et al.*, 1995]. ARM is now establishing a site on the North Slope of Alaska.

The Antarctic Plateau is an ideal location for acquiring spectral radiance data for testing radiative transfer models. Since the atmosphere is so cold and dry ($\leq$1 mm of precipitable water), the overlap of the emission spectrum of water vapor with that of other gases is greatly reduced. Therefore the spectral signatures of other important infrared emitters, namely, CO_2, O_3, CH_4, and N_2O, are quite distinct. In addition, the low atmospheric temperatures provide an extreme test case for testing models. Even in summer the atmosphere is colder and drier than the sub-Arctic winter, the coldest of the five AFGL model atmospheres. The radiation conditions at the surface of the Antarctic Plateau in winter are similar to those at the tropopause at lower latitudes. Routine operations at South Pole Station provide good ancillary data for characterizing the atmosphere throughout the year. The South Pole Weather Office (SPWO) launches radiosondes once or twice per day and makes surface weather observations at least every 6 hours. The Climate Monitoring and Diagnostics Laboratory (CMDL) of the National Oceanic and Atmospheric Administration (NOAA) provides continuous near-surface concentrations of several radiatively active trace gases, as well as ozonesonde profiles once or twice per week.

Many previous Antarctic field programs have reported measurements of broadband radiation fluxes [*Hanson*, 1960; *Hanson and Rubin*, 1962; *Rusin*, 1964; *Kopanev*, 1967; *Kuhn et al.*, 1977; *Yamanouchi et al.*, 1982; *Carroll*, 1982; *Yamanouchi and Kawaguchi*, 1984]. Such broadband measurements, however, are not useful for identifying defects in radiative transfer models. Here our focus is instead on how the radiance varies across the infrared spectrum. In this paper we describe a data set taken at South Pole Station throughout the year of 1992, consisting of spectral infrared radiances together with observations from radiosondes and other instruments to characterize the atmosphere. Particular attention is given to the calibration and uncertainty associated with the radiation measurements. The calibration procedure described here is an improvement over that of *Van Allen et al.* [1996], which used the same instrument at South Pole Station. Their experiment was designed to study stratospheric chemistry, which did not require the level of accuracy needed here for SPECTRE-type comparisons.

The uncertainties associated with characterizing the atmosphere are also estimated, particularly with regard to temperature and humidity variations in the near-surface layer. Three test cases are constructed, using the highest-quality measurements from the data set, representing the meteorological and infrared radiation conditions in summer, winter, and spring under clear sky. These test cases are used to compare the spectral infrared radiances with calculations of the line-by-line radiative transfer model (LBLRTM) [*Clough et al.*, 1992]. A brief description of LBLRTM is given below as it is applied to this work, including how the model calculations were adjusted for instrumental effects, so that the model results can be compared directly with the observations. The radiance error in the LBLRTM calculations induced by uncertainties in the ancillary data is estimated; the major sources of error are identified for summer and winter conditions. The comparisons for our six test cases (two viewing angles on each of 3 days) are shown, and portions of the spectrum are examined in detail.

2. Field Program

Spectral radiance was measured by a Fourier transform interferometer (FTIR), manufactured by Bomem, Inc., and modified at the University of Denver (UD) for outdoor operation at South Pole. It had been successfully operated through a previous winter at South Pole for the purpose of determining concentrations of atmospheric gases important to ozone chemistry [*Murcray and Heuberger*, 1990, 1991, 1992]. The radiance spectrum was measured at viewing zenith angles of 45° and 75°, and also often at 60°, every 12 hours throughout the year except during blizzard conditions.

The state of the atmosphere is characterized by using various sources of data. Visual sky observations were made by Warren during each FTIR measurement, as well as routinely every 6 hours by the SPWO observers. Vertical profiles of temperature, water vapor, and ozone are constructed by using a combination of radiosonde data from SPWO and CMDL, plus satellite data from the Upper Atmosphere Research Satellite (UARS) [*Reber et al.*, 1993]. Tropospheric concentrations of carbon dioxide, methane, nitrous oxide, and chlorofluorocarbons were obtained from in situ measurements made at the surface by CMDL, and stratospheric concentrations were obtained from UARS.

3. Selection of Test Cases

Three days were selected for comparison of spectral radiance measurements to radiative transfer models: January 17, 1992, May 1, 1992, and October 5, 1992. For each day the calibrated radiances at viewing zenith angles of 45° and 75° are determined. The three primary criteria for selection were clear skies with minimal visually observed atmospheric ice crystals, well-calibrated spectral radiance measurements, and time of year. The summer and winter cases were chosen to span the full range of atmospheric conditions over South Pole; the springtime case represents an atmosphere with a depleted ozone profile. Secondary selection criteria include availability of high-quality radiosonde and ozonesonde information and minimal time between the radiosonde launch and the spectral radiance measurements (Table 1). The seasons at South Pole are defined by the annual cycle of surface temperature [*Schwerdtfeger*, 1970; *Warren*, 1996]: summer

Table 1. Characteristics of the Interferometric Measurements and Model Atmospheres for the Three Selected Test Cases

Date	Jan 17, 1992	May 1, 1992	5 Oct 1992
Representative season	summer	winter	spring
Start time of FTIR measurement, UT	2215	2230	1021
Time of radiosonde launch, UT	2214	2131	0941
Total downward longwave flux, W m^{-2}	121	76	78
Surface air temperature, °C	-32	-66	-62
Inversion strength, K	5	29	25
Total column water vapor, mm of precipitable water	1.0	0.3	0.3
Carbon dioxide mixing ratio, ppmv	353	353	355
Total column ozone, DU	287	247	147
Methane mixing ratio at the surface, ppbv	1654	1661	1679
Nitrous oxide mixing ratio at the surface, ppbv	308.9	308.6	309.1
CFC-11 mixing ratio at the surface, pptv	265	265	267
CFC-12 mixing ratio at the surface, pptv	491	494	498

DU, Dobson Unit; 1 DU = 0.001 atm cm.

(December-January), autumn (February-March), winter (April-September), and spring (October-November).

On the three days chosen, no visual clouds were observed in any portion of the sky by either the SPWO or Warren. The May 1 case was chosen partly because the amount of clear-sky ice crystal precipitation ("diamond dust") was slight and partly because polar stratospheric clouds (PSCs) normally are not present until later in the winter [*Poole and Pitts*, 1994]. Polar stratospheric clouds are hard to detect visually from the surface during nighttime, but the assumption that they were absent on May 1 is supported by the lidar data discussed by *Cacciani et al.* [1993].

The primary factor controlling the availability of good sonde data is the type of balloon used. During the winter, plastic balloons were used alternately with standard rubber balloons; plastic balloons typically reach higher altitudes (about 30 km) before bursting but are more expensive. Test cases were chosen for days on which the balloon reached high altitude.

4. Spectral Radiance Measurements

4.1 Data

A Michelson-type interferometer was used: Bomem model MB-100 with electronics upgraded to an MB-120. Data acquisition from the instrument is controlled by an IBM-PC compatible computer using software developed by Bomem and UD. Modifications made at UD for operation in Antarctica include the following. A mercury-cadmium-telluride (MCT) semiconductor detector, cooled by liquid nitrogen, was installed for high sensitivity at thermal infrared wavelengths. The liquid nitrogen was supplied by a Joule-Thompson expansion cooler using nitrogen gas from high-pressure storage bottles. An external mirror assembly was attached to the interferometer, enabling it to view two external calibration sources and the sky at three zenith angles.

The interferometer is a two-input, two-output instrument. The detector, placed at one of the output ports, records the superposition of infrared radiation from the two input ports, one of which is an internal reference source; the other is the scene. The output varies as a function of the optical path difference of the scanning mirror; its DC offset is suppressed by the interferometer's electronics by coupling to the variable portion of the signal [*Beer*, 1992, equation (1.14b)]. The total optical path difference is 16,384 (633 nm) = 1.04 cm; the wavelength of the interferometer's laser is 633 nm. Typically, the mirror scans about 50 to 100 times successively, with the output from all scans being averaged by a process called co-adding. (This number of co-added scans was necessary to ensure an adequate signal-to-noise ratio for UD's research [*Van Allen et al.*, 1996].) The final co-added record is called an interferogram. The Bomem software apodizes the interferogram using the Hann-window function [*Press et al.*, 1992], and performs a Fourier transform, producing an uncalibrated spectrum for that individual measurement. The spectral resolution of the transformed data is 1 cm^{-1} (full width at half maximum). The spectral bandwidth of the instrument is limited by the response of the MCT detector and the bandpass of the beamsplitter to the range 550-1667 cm^{-1}, or 6-18 μm. At these limiting wavenumbers the response is about 10% of the peak response at 900 cm^{-1}.

During a typical spectral radiance measurement the interferometer views four or five different scenes successively. A "measurement sequence" consists of viewing zenith angles of 45° and 75° (and often 60°), bracketed by views of calibration sources: one at ambient air temperature and another at about 45 K above ambient. A typical measurement sequence takes 20-30 min. The calibration sources are grooved copper plates painted with Aeroglaze Z306, a polyurethane coating. Each source has two thermistors imbedded in the back of the copper disk, sensing its temperature. The cold source has one thermistor at the center of the disk and the other on the periphery. The warm source has a resistive heater attached to the center of its back surface, to elevate its temperature above ambient. One of its thermistors is therefore slightly off center, while the other is on the periphery.

Measurement sequences were performed approximately every 12 hours throughout the year at South Pole and during most routine radiosonde launches made by the SPWO. Measurement

sequences were taken more frequently when the sky was clear, and special observations were made during some ozonesonde and water vapor sonde launches. "Housekeeping" information was recorded routinely during each sequence, consisting primarily of temperature measurements of various parts of the interferometer. These measurements were used to select test cases with good thermal stability, in which the instrument temperature drifted by less than 0.1 K during the measurement sequence [*Walden*, 1995].

The interferometer was mounted atop the Skylab building at an elevation of approximately 10 m above the upwind snow surface. The instrument was housed in about 10 cm of styrofoam insulation, while the external mirror assembly was exposed to the ambient temperature. Thus the internal temperature of the interferometer varied only slowly as the ambient temperature changed.

4.2 Calibration

The method of *Revercomb et al.* [1988] is used to calibrate measurements of the sky. An uncalibrated spectrum, C', can be written as a linear function of the measured radiance, L, as

$$C' = r\left[L + L^{o}e^{i\phi^{o}}\right]e^{i\phi}, \tag{1}$$

where r is the instrument response function of the interferometer, L^o represents the spectral offset radiance from the instrument itself, ϕ is the phase response of the instrument due to optical and electrical dispersion, and ϕ^o is any anomalous phase incorporated into the offset radiance [*Revercomb et al.*, 1988]. All the variables are functions of frequency. Subscripts w, c, and s are applied to C' and L, referring to warm, cold, and sky (or scene). The uncalibrated spectra for the warm and cold calibration sources, C_w' and C_c', are used to calibrate the measurements of the sky, C_s', by taking the real part of the ratio of difference spectra and solving for the scene radiance, L_s, giving

$$L_s = \gamma[L_w - L_c] + L_c, \tag{2}$$

where

$$\gamma = \mathrm{Re}\left[\frac{C_s' - C_c'}{C_w' - C_c'}\right]. \tag{3}$$

L_w and L_c are the radiances emitted and reflected from the calibration sources:

$$L_j = \varepsilon_j B(T_j) + (1-\varepsilon_j)B(T_{ambient}), \tag{4}$$

where j is either w or c. B(T) represents the Planck radiance at a particular frequency for a given temperature T, T_j is the temperature of the emitting surface of the source, ε_j is the spectral emissivity of the source, and $T_{ambient}$ is the temperature of the ambient outside air.

There are implicit assumptions in equation (1). First, the output from the interferometer's detector is assumed to be linearly related to the input radiance into the interferometer. The possibility of nonlinearities in the detector is not considered in this study, since any resulting bias is probably small compared with the overall radiance uncertainty discussed below.

In addition, the assumption of thermal stability means that the offset radiance $L^oe^{i\phi^o}$ is constant within a measurement sequence, so that it can be eliminated by the taking the difference of measurements C', which results in the numerator and denominator of equation (3). The maximum acceptable level of thermal drift of the interferometer during measurement sequences to be used for test cases was chosen such that any radiance errors resulting from thermal drift are negligible compared with those from other error sources. However, a procedure for adjusting measurement sequences with large thermal drift has been developed by *Walden* [1995].

The radiances from the calibration sources, L_w and L_c, must be known accurately, independent of the measurements, for proper calibration of atmospheric radiances. Thus the accuracy of the final calibrated radiances depends on accurate specification of the source temperature and emissivity. The uncertainties in these temperatures and emissivities must also be assessed to estimate the uncertainty in calibrated radiances. The source temperatures and emissivities described below differ from those used by *Van Allen et al.* [1996].

4.2.1 Temperature of the calibration sources. The temperature of each calibration source is measured by two thermistors that were calibrated to a temperature reference of the National Institute of Standards and Technology (NIST) by the manufacturer (Yellow Springs Instruments, Inc., Yellow Springs, Ohio). The electronics used to measure the source temperatures were checked by substituting four different high-precision resistors in place of each thermistor. The resistors were chosen to represent a range of temperatures far exceeding the range experienced at South Pole. The voltage recorded by the electronics was converted back to a resistance value, which was then compared with the value of the precision resistors. Analysis of this cross-check procedure indicated that a small additional resistance needed to be added to the inferred resistances to reconcile them with the actual values. In the conversion of resistance to temperature this correction was significant when the resistance being measured was small (less than 1000 ohms). The additional resistance ranged from 9 to 75 ohms and varied from channel to channel within the data acquisition system. Using the thermistor manufacturer's conversion from resistance to temperature, we derived temperature corrections for each thermistor. Figure 1 shows the corrections for the four thermistors on the calibration sources over the range of temperature values experienced by these sources at South Pole in 1992. The corrections are significant at high temperatures, or low thermistor resistance. The corrections are 0.6 K and 1.3 K for the cold source thermistors at their maximum yearly temperature of -10°C, and 0.3 K and 1.3 K for the warm source thermistors at +35°C.

Figure 2a shows the difference in temperature reported by the two thermistors on the cold calibration source. Since the cold source is at ambient outside temperature, the two thermistors should agree. True temperature differences between the thermistors would be due to random variation of environmental conditions such as wind speed and direction, causing only random scatter in the data. Figure 2a shows instead a consistent pattern of deviation with small scatter; the deviation exceeds the manufacturer's tolerance limit at high temperatures. Figure 2b shows that after correcting for the thermistor electronics bias the cold source temperatures agree well for the entire temperature range throughout the year, thus validating the correction procedure. The true cold source temperature, T_c, is then estimated by averaging T_4' and T_{10}', where the prime indicates that the correction for the electronics bias has been applied:

$$T_4' \equiv T_4 + \Delta_{e4}, \tag{5}$$

where Δ_{e4} is the temperature correction for the thermistor electronics bias of channel 4. A similar expression exists for T_{10}'.

A similar analysis of the warm source is not possible since temperature gradients do exist within the heated plate, but the success

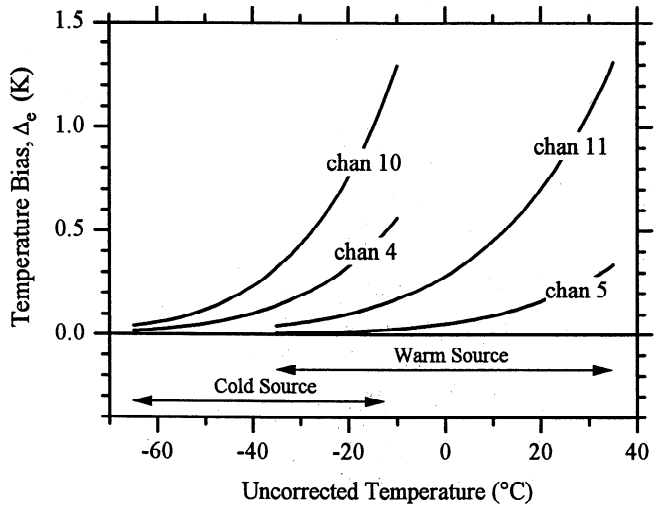

Figure 1. Thermistor electronics temperature bias (Δ_e) for the individual thermistors in the infrared calibration sources. The bias is shown for the range of temperatures experienced at South Pole during 1992. The thermistors are designated by their housekeeping channel number: channels 4 and 10 for the cold source thermistors and channels 5 and 11 for the warm source thermistors. Channels 4, 10, and 11 are 300-ohm thermistors (YSI 44002); channel 5 is a 3000-ohm thermistor (YSI 44005). All thermistors were manufactured by Yellow Springs Instruments, Inc., Yellow Springs, Ohio.

of the electronics bias correction procedure for the cold source argues for its validity in general. We therefore apply the electronics bias correction to the warm source thermistors, T_5 and T_{11}. However, for the warm source there is an additional correction that must be applied due to thermal gradients within this source. Figure 3a shows that there is a significant temperature difference between the two thermistors on the warm source, which increases as the source temperature (e.g., T_5') rises above ambient (T_c). This behavior is expected because all thermal gradients in the source should be proportional to the difference between its temperature and ambient. Since the two thermistors are at different temperatures, it was necessary to decide which sensor has better accuracy. T_5' was chosen for two main reasons [*Walden*, 1995]: it has better sensitivity over most of the range of temperatures experienced during 1992, and the thermistor electronics temperature bias is much smaller for channel 5 than for channel 11 (Figure 1).

In addition to the radial temperature gradient between the thermistors shown in Figure 3a, there is evidence of a temperature difference between T_5' and the temperature of the emitting surface of the warm source as viewed by the interferometer. Three independent analyses described by *Walden* [1995, Appendix A] indicate that the portion of the source viewed by the interferometer is actually warmer than T_5'. This higher temperature is due to the location of the warm source's resistive heater in relation to its thermistors mentioned above, assuming that the interferometer views the center of the copper plate. The results from these analyses are reproduced in Figure 3b. The temperature difference increases as the warm source becomes increasingly warmer than ambient.

A functional form for the thermal gradient temperature bias, Δ_g, was determined by performing a linear regression fit to the data shown in Figure 3b. The fit was forced through the origin, since no thermal gradients exist within the calibration source when it is at ambient temperature. Our final estimate for the temperature of the viewed portion of the warm calibration source, T_w, is then obtained by applying corrections for both the thermistor electronics (Δ_{e5}) and thermal gradient biases, or

$$T_w \equiv T_5' + \Delta_g = T_5 + \Delta_{e5} + \Delta_g . \quad (6)$$

The larger of these two corrections is Δ_g. For the range of warm source temperatures experienced during the year-long field experiment, Δ_g was in the range 1-4 K, whereas Δ_{e5} was at most 0.3 K.

4.2.2 Emissivity of the calibration sources. The spectral emissivity of the UD calibration sources was not directly measured but was inferred from the measured emissivity of a similar source built by Quantic Industries, Inc. (San Carlos, California) while Walden worked there. Both the UD and Quantic sources are grooved copper plates, coated with the same black paint, Aeroglaze Z306. The emissivity of nongrooved plates (constructed independently by Quantic and H. E. Revercomb's group at the University of Wisconsin, but both painted with Aeroglaze) compare well, indicating that perhaps the emissivity in the spectral range 750-1300 cm^{-1} (the central portion of the interferometer's bandwidth) is not highly sensitive to the paint thickness [*Walden*, 1995, Appendix A]. The emissivity of the Quantic grooved source in this spectral region was the value used in deriving the thermal gradient bias described above.

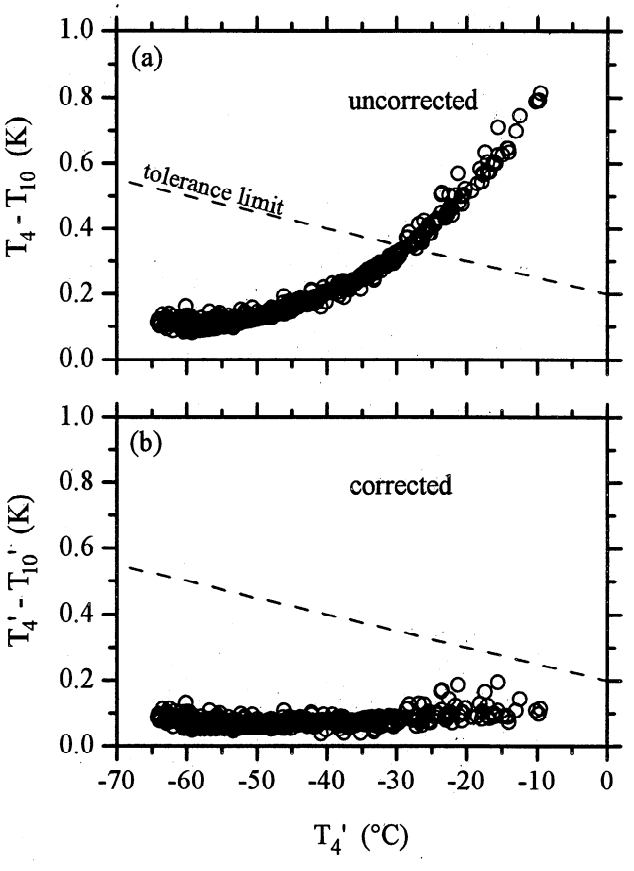

Figure 2. Temperature difference between the cold calibration source thermistors (a) before and (b) after being corrected for the thermistor electronics temperature bias. T_4 and T_{10} are the uncorrected temperatures from two thermistors recorded in the housekeeping channels 4 and 10. T_4' and T_{10}' are the corresponding corrected temperatures. The dashed line is the thermistor manufacturer's interchangeability tolerance, defined as the maximum difference that can occur when two or more thermistors are used to make the same measurement.

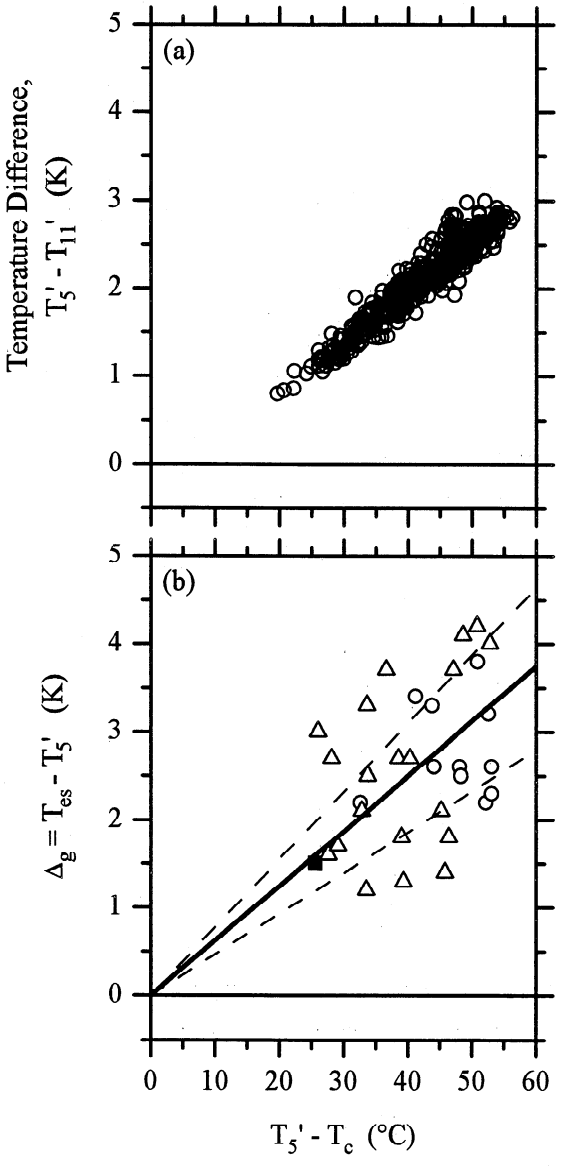

Figure 3. Temperature gradients within the warm calibration source. (a) Temperature difference between the two warm source thermistors plotted against the temperature difference between the warm and cold source temperatures. Since the cold source is at the outside air temperature (T_c), the abscissa represents the degree to which the warm source is above ambient. T_5' and T_{11}' are the temperatures from housekeeping channels 5 and 11, corrected for the thermistor electronics bias. (b) Thermal gradient temperature bias, Δ_g, i.e., the difference in temperature between the emitting surface of the warm source (T_{es}) viewed by the interferometer and T_5'. The open circles were derived from the supplemental calibrations using a third calibration source, the solid square is from the laboratory test performed by the University of Denver, and the open triangles are from the analysis using the secant method [*Walden*, 1995]. The solid line is a linear regression fit of the data forced through the origin [$\Delta_g = 0.062(T_5' - T_c)$]. The dashed lines indicate the uncertainty in the best fit slope, which is ±25%.

At the shortwave and longwave ends of the interferometer's bandwidth (550-750 cm^{-1} and 1300-1667 cm^{-1}) the Quantic source is not a good proxy for the UD sources because the emissivity may be sensitive to the paint thickness; the emissivities of the nongrooved plates in these spectral regions are quite different. In these spectral regions the emissivity of the UD sources is determined in the following way, using monthly supplemental calibration data taken with a third infrared source, a conical cavity constructed by the University of Wisconsin (hereinafter referred to as the WI source). (The three thermistors used in the WI source had been calibrated to a NIST temperature reference.) The instrument response function given by *Revercomb et al.* [1988] is determined as

$$r = \frac{|C_i' - C_j'|}{L_i - L_j}. \tag{7}$$

where i and j can represent either the UD sources (w and c) or a series of measurements made with the WI source at different temperatures. Under the assumption that the ambient and instrument temperatures remain constant during the measurement sequence using each experimental setup, equation (4) can be substituted into equation (7) to obtain

$$\beta \equiv r\varepsilon = \frac{|C_i' - C_j'|}{B(T_i) - B(T_j)}. \tag{8}$$

The quantity β can be determined by using either the two UD sources (β_{UD}) or the WI source (β_{WI}). The ratio, β_{UD}/β_{WI}, yields the ratio of the spectral emissivities of the sources, $\varepsilon_{UD}/\varepsilon_{WI}$. Here ε_{WI} is assumed to be 0.9956 independent of wavenumber, as measured at the University of Wisconsin (R. O. Knuteson, personal communication, 1994), and thus ε_{UD} is determined.

Figure 4 shows the spectral emissivity of the Quantic source and the calibration sources used in this study. The emissivity of the calibration sources is generally between 0.97 and 0.99 but has significant features at 600, 1600, and 1650 cm^{-1}. Accounting for these spectral features improves the agreement between the calibrated radiances and radiative transfer calculations described below.

4.3 Calibrated Spectra

Figure 5 shows the calibrated spectra for the six comparison test cases. The contributions of several greenhouse gases are distinctly visible as a result of the small amount of atmospheric water vapor. The 667-cm^{-1} band of carbon dioxide is bounded by the atmospheric window region at 800-1200 cm^{-1} and by the rotational band of water vapor at wavenumbers ν < 600 cm^{-1}. The

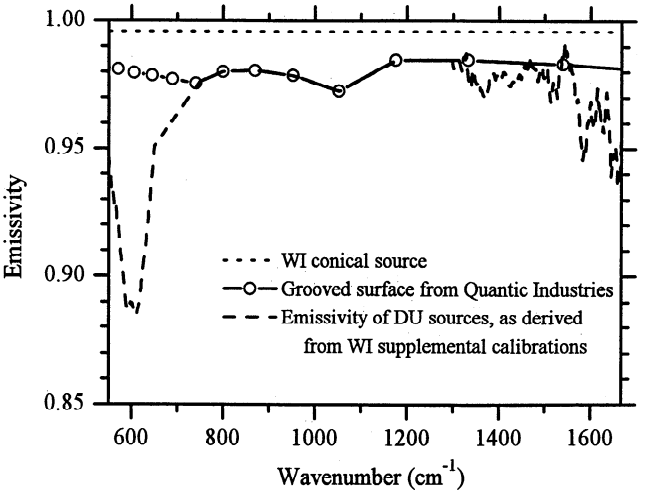

Figure 4. Spectral emissivities of the calibration sources.

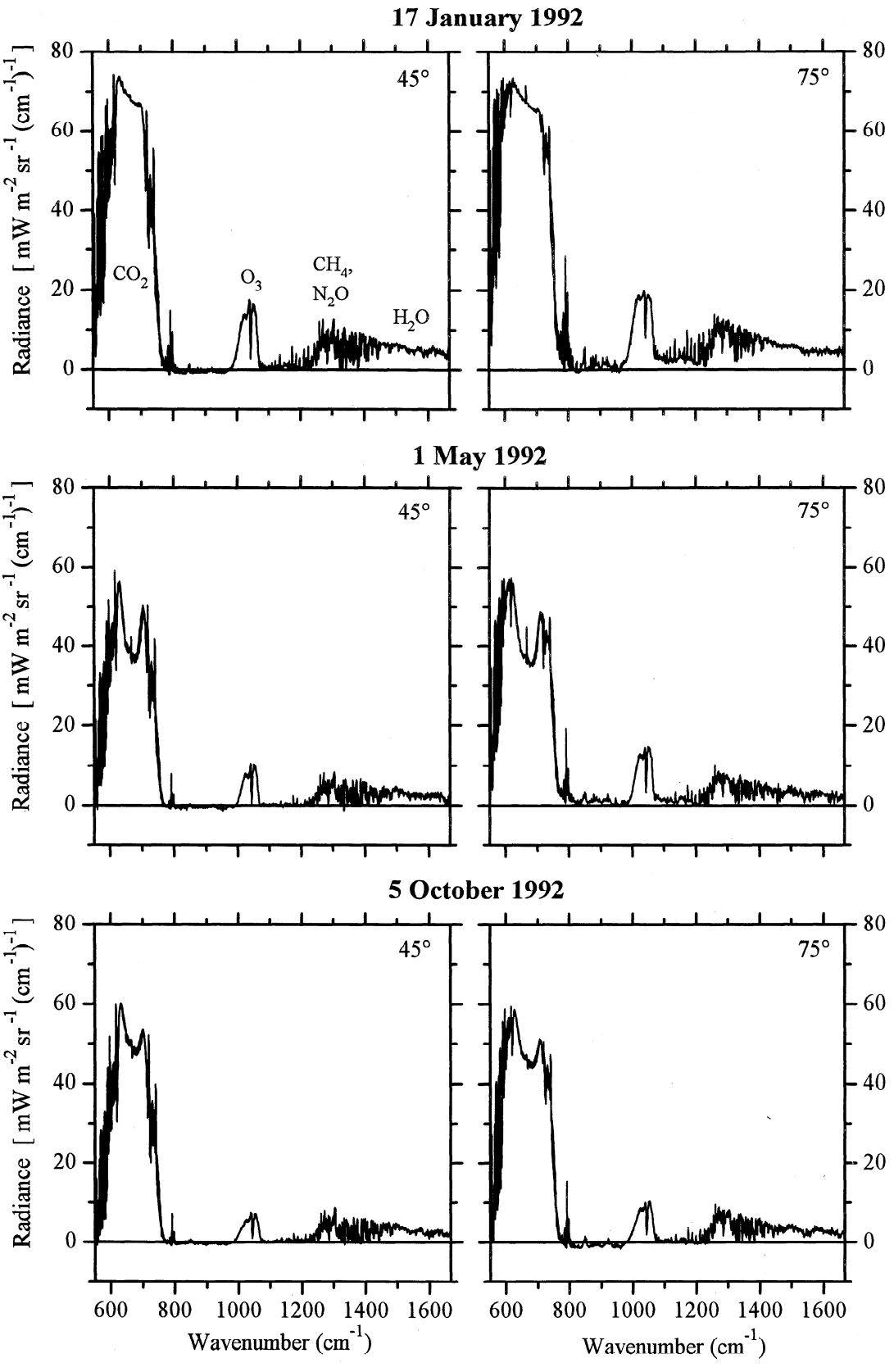

Figure 5. Calibrated radiances for the six test cases. The viewing zenith angles are 45° and 75° for the 3 selected days.

effect of the strong near-surface temperature inversion in winter (May) and spring (October) is most prominent in the center of the carbon dioxide band. Between 800 and 1200 cm^{-1}, emission from the water vapor continuum is very small. The 1042-cm^{-1} ozone band stands out in the middle of the window region. Methane and nitrous oxide have emission bands around 1275 cm^{-1}, and the 1600-cm^{-1} (6.3 μm) band of water vapor is visible at ν>1350 cm^{-1}.

The total downward infrared fluxes, as measured by a pyrgeometer near the times of the spectral radiance measurements, are given in Table 1.

4.4 Radiance Uncertainties

Variables entering the calibration equations ((2), (3), and (4)) must be assessed for how their uncertainties propagate to uncertainty in the calibrated radiances. The interferometric measurements (C_w', C_s', C_c') are subject to inherent instrument noise associated with the detector and its electronics, which when converted to radiance units is called the noise equivalent spectral radiance (NESR). Radiance errors from the calibration sources (L_w and L_c) are due to uncertainties in the temperatures (σ_T) and emissivities (σ_ε) of the emitting surfaces. The total estimated radiance error σ_L is given as

$$\sigma^2_L = \sigma^2_{LT} + \sigma^2_{L\varepsilon} + NESR^2, \quad (9)$$

where we use σ_{LT} and $\sigma_{L\varepsilon}$ for the radiance uncertainties due to temperature and emissivity uncertainties. All the quantities have units of radiance. There is additional error associated with the thermal stability of the interferometer, but on the 3 days used in this study this error is negligible compared with those listed in equation (9).

To determine σ_{LT}, we first estimate the temperature uncertainties in the warm and cold calibration sources, σ_{Tw} and σ_{Tc}. The sky radiance is computed from a calibration using the standard temperatures, T_w and T_c, and from another calibration using $T_w - \sigma_{Tw}$ and $T_c + \sigma_{Tc}$. The difference between these two radiances is taken as an estimate of the maximum radiance error due to temperature, since if both σ_{Tw} and σ_{Tc} were added or subtracted from their respective temperatures, the radiance error would be less than that for the case described.

The dominant contributor to σ_{Tw} is the uncertainty in the thermal gradient temperature bias, Δ_g, for the warm calibration source. The uncertainty in Δ_g is proportional to the uncertainty in the slope shown in Figure 3b and also depends on the temperature difference ΔT between the warm and cold sources, i.e., between the warm source and ambient air. The farther the warm source is above ambient, the larger Δ_g and its uncertainty; σ_{Tw} increases from 0.4°C at ΔT = 25 K to 0.8°C at ΔT = 55 K.

The uncertainty in the cold source temperature, σ_{Tc}, depends on both the uncertainty given by the manufacturer for individual thermistors and the uncertainty in the thermistor electronics bias correction. The manufacturer's uncertainty dominates at low temperatures (< -50°C); the uncertainty (1σ) for these thermistors (YSI 44002) increases from about 0.1°C at 0°C to 0.2°C at -80°C. At high temperatures (> -30°C), the uncertainty in the thermistor electronics bias dominates.

The radiance error due to temperature uncertainties, σ_{LT}, is shown in Figure 6a for the worst (January 17 at 45°) and best (May 1 at 75°) error conditions of the six spectra shown in Figure 5. It is largest in the spectral regions where the absolute radiance is small, i.e., where the atmosphere is relatively transparent. This is because errors in the derived sky radiance induced by the errors in the calibration sources are greater when extrapolated to lower

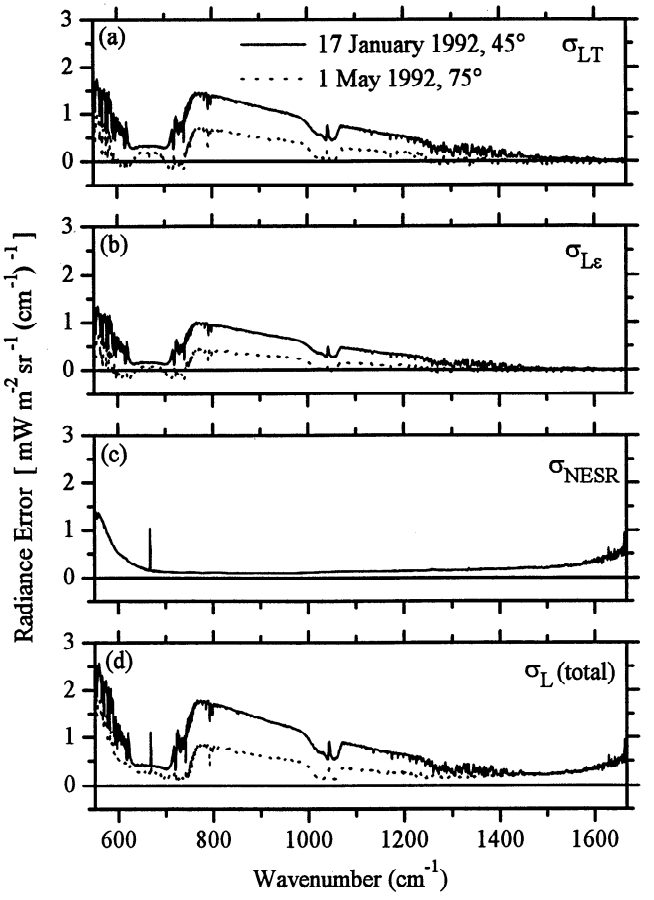

Figure 6. Estimated radiance errors for two of the calibrated spectra shown in Figure 5. The various panels represent contributions to the radiance error listed in equation (9). Here σ_{NESR} is identical for January 17 and May 1.

radiance values. This situation is especially true in summer when the calibration source temperatures are relatively higher than they are in winter when compared with the brightness temperature of the sky.

The radiance error due to the uncertainty in the calibration source emissivities is determined by taking the difference in radiance between a calibration using ε and a calibration using $\varepsilon + \sigma_\varepsilon$. A generous estimate of σ_ε is used here; $\sigma_\varepsilon = \pm 0.015$. The corresponding radiance error $\sigma_{L\varepsilon}$ is shown in Figure 6b.

The NESR was determined by *Walden* [1995]; it is significant primarily at the limits of the interferometer's bandwidth (Figure 6c), as a result of the roll-off of the instrument response. The chosen bandwidth of the instrument restricts the NESR to an acceptable level for this study.

The total radiance error (Figure 6d) shows generally the same spectral characteristics as σ_{LT} and $\sigma_{L\varepsilon}$. The radiance error due to temperature uncertainty σ_{LT} constitutes most of the total error, but $\sigma_{L\varepsilon}$ provides a sizable contribution. The effect of the NESR becomes significant at the ends of the instrument's bandpass and dominates at high wavenumbers.

5. Specification of Atmospheric Composition and Structure

Model atmospheres are constructed for the times that spectral radiance was measured on January 17, May 1, and October 5. The

trace gases included in our model atmospheres are water vapor, carbon dioxide, ozone, methane, nitrous oxide, oxygen, CCl_3F (CFC-11), and CCl_2F_2 (CFC-12). They are included either because they are major infrared emitters in the atmosphere (water vapor, carbon dioxide, ozone, methane, nitrous oxide) or because their concentrations are readily available at South Pole Station (CFC-11, CFC-12). The values are summarized in Table 1 along with other information about the three selected test cases. Detailed information on each model atmospheric profile and their associated uncertainties is given by *Walden* [1995].

To select times when the sky conditions were most clear, we consult the visual sky observations made by the SPWO and by Warren. Clouds were detected at night when they were illuminated by moonlight or, in the absence of moonlight, by their obscuration of familiar stars. Slight diamond dust was observed by Warren in the interferometer's field of view on May 1 but not on January 17 and October 5. Sunlight was available for the observations on January 1 and October 5. Both the Sun and the moon were below the horizon on May 1.

5.1 Temperature

The temperature profiles in the near-surface layer, from the surface (2.8 km above sea level) to 4 km, were obtained from SPWO radiosondes, corrected for thermal lag of the radiosonde's thermistor by the method of *Mahesh et al.* [1997]. The uncertainty in this correction depends upon how rapidly the temperature structure changes with altitude and is therefore greater in winter (±0.6°C) than in summer (±0.2°C). Another concern is the temporal constancy of the temperature within the inversion layer, since the temperatures were not measured coincidentally with the spectral radiances; the times of the FTIR measurement and the radiosonde launch are shown in Table 1. For May 1 the uncertainty is estimated to be 0.6°C, and 0.9°C for October 5 [*Walden*, 1995]. The total uncertainty in the near-surface temperature profile is obtained by combining the two uncertainties discussed above with the inherent temperature uncertainty (±0.5°C) given by the manufacturer of the sonde (Atmospheric Instrumentation Research, Inc., Boulder, Colorado). For the near-surface layer these are ±0.5°C, ±1.0°C, and ±1.2°C for January 17, May 1, and October 5.

The temperature profiles above 4 km are derived from the SPWO radiosonde data and data from the cryogenic limb array etalon spectrometer (CLAES) and the Halogen Occultation Experiment (HALOE) aboard the UARS [*Roche et al.*, 1993; *Russell et al.*, 1993; *Hervig et al.*, 1995]. The radiosondes for our three case studies reached altitudes of about 30 km. The temperature uncertainty between 4 and 30 km is set to ±0.5°C, the manufacturer's estimate. Temperatures between 30 km and 60 km were obtained from the UARS data archive at the Distributed Active Archive Center (DAAC) at Goddard Space Flight Center. The time reference data product (3AT) was used. The retrieved temperatures from CLAES have better accuracy (1°-2°C) than those from HALOE (2°-5°C) and are therefore used whenever available. Only data with positive quality values are used, meaning that the data are based on actual atmospheric measurements rather than climatology. Even though the UARS instruments view only to a maximum southern latitude of 80°S, the temperatures from the radiosondes generally agree with those from UARS, where they overlap, to within the estimated uncertainties at the 2σ level. This agreement is found as well for water vapor and ozone discussed below.

The temperature profiles for the three model atmospheres are shown in the first two columns of Figure 7; the second column shows the near-surface layer with an expanded vertical scale. The atmosphere is warmest at all altitudes on January 17. By May 1 the stratosphere has cooled as a result of the lack of sunlight. In October the temperatures between 14 and 17 km are below 195 K, cold enough for the formation of type I PSCs. The near-surface temperature structure on January 17 shows a small surface-based inversion, indicating that solar heating of the surface is not providing enough energy to compensate for the loss of longwave radiation. On May 1 with no Sun, and October 5 with low Sun, the surface-based inversion is well developed.

5.2 Water Vapor

Water vapor is an extremely important atmospheric constituent, but it is the least well known of the gases measured at South Pole and used in this study. The tethered kite experiments described by *Mahesh et al.* [1997] are used to gain insight into the water vapor content of the near-surface atmosphere. Despite the fact that the carbon hygristors used for these tests were calibrated only down to -40°C, the data suggest that the relative humidity with respect to ice (RH_i) is close to saturation in the near-surface layer. In fact, *Schwerdtfeger* [1970; 1984] took the frequent occurrence of diamond dust ice crystals as evidence that the lower atmosphere must be at least saturated with respect to ice. On the basis of the tethered hygristor data we assume that the near-surface inversion layer is saturated with respect to ice, and we bound the atmospheric relative humidity (with respect to ice) in this layer with a range of 90-110%.

Tropospheric humidity was measured by three different instruments: carbon hygristors used routinely by the SPWO, two frost-point hygrometers launched by NOAA, and capacitive-type Vaisala Humicaps that were packaged with the frost-point hygrometers and ozonesondes. Like the carbon hygristors the Humicaps are calibrated only down to -40°C. The frost-point hygrometers are designed to measure stratospheric humidities and thus are tuned for low absolute humidities (S. J. Oltmans, personal communication, 1993).

On the basis of a small set of intercomparisons between these various instruments it is impossible to draw firm conclusions about the variability of tropospheric humidity. However, the data suggest that the troposphere can be either near saturation or substantially subsaturated in the winter [*Walden*, 1995]. Because there is no agreement between the SPWO carbon hygristor and the Vaisala Humicap, some judgment is needed in specification of humidity for the model atmospheres, taking into account the atmospheric processes occurring over the Antarctic Plateau. For all three of our model atmospheres, RH_i from 4 to 7 km is assumed to be 75% ± 25%.

The microwave limb sounder (MLS) and HALOE instruments from the UARS are used here to provide water vapor information from about 30 to 60 km, or 100 to 0.1 mbar. Comparisons between MLS data and the two NOAA-CMDL frost-point hygrometers launched from South Pole in 1992 are very good despite the fact that the UARS data are for lower latitudes [*Walden*, 1995].

Figure 7 (right) shows the humidity profiles for the three model atmospheres. In all cases the troposphere is more humid than the upper atmosphere. The May and October cases have less water vapor in the near-surface layer and the troposphere because of the extreme low temperatures. The total column amount is 1 mm of

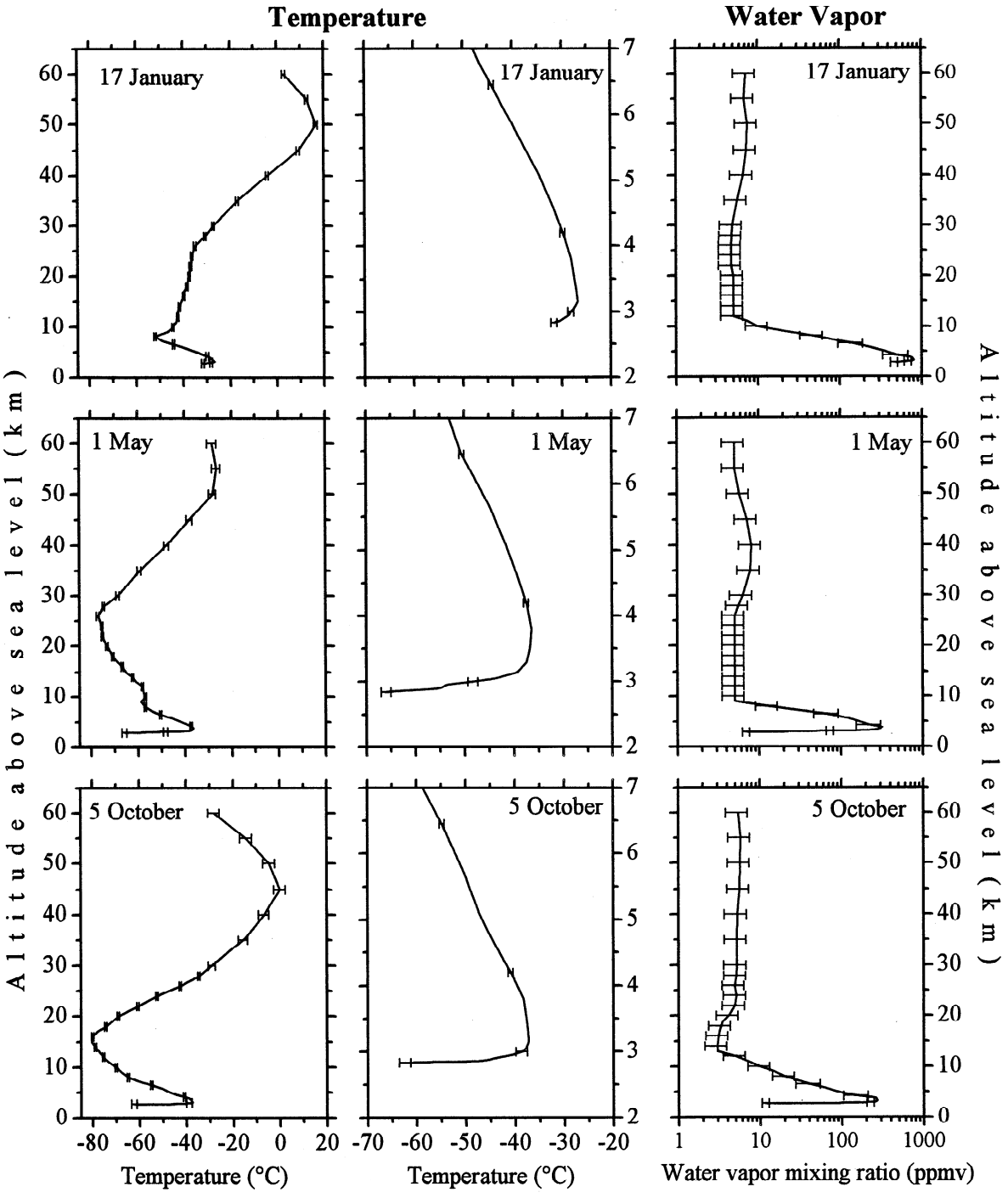

Figure 7. Vertical temperature and humidity profiles for the three model atmospheres: (left) temperature through the entire atmosphere; (middle) temperature in the first 4 km above the surface, and (right) water vapor profiles for the entire atmosphere. Error bars are discussed in the text.

precipitable water on January 17, and 0.3 mm for May 1 and October 5.

5.3 Other Gases

Air samples were collected in flasks and analyzed for CO_2 by NOAA-CMDL [*Komhyr et al.*, 1983, 1985; *Thoning et al.*, 1987]. The values on January 17, May 1, and October 5 were 353.5, 353.5, and 355.0 ppmv, respectively. These mixing ratios are used at all altitudes in the model atmospheres, since CO_2 is well mixed in the troposphere and stratosphere. As a conservative estimate of the uncertainty we used 2 ppmv, the range of the seasonal cycle.

Ozone profiles were obtained from 68 ozonesondes launched by NOAA-CMDL in 1992, approximately once per week through most of the year but once every 3 days in spring. To specify ozone profiles for the model atmospheres, we interpolate linearly in time between the measured profiles. Since the ozonesondes typically rise only to about 30 km, ozone amounts for 30-60 km are obtained from MLS (205-GHz channel), CLAES (780-cm^{-1} channel), and HALOE. Overlap of the sonde data with the satellite

data was excellent on January 17 (MLS) and May 1 (CLAES) and good on October 5 (HALOE). For these 3 days, the integrated ozone profiles agree to within 5% with the total ozone reported by CMDL's Dobson spectrophotometer at South Pole and the total ozone mapping spectrometer aboard the Nimbus 7 satellite.

The ozone profiles for the three model atmospheres are shown in Figure 8. On October 5, severe depletion is seen between 12 and 18 km, coincident with the low temperatures in this region. The total column ozone amounts for January 17, May 1, and October 5 are 287, 247, and 147 Dobson units (DU).

Methane mixing ratios at the surface were obtained by analyzing flask samples [*Steele et al.*, 1987; *Lang et al.*, 1990a,b], collected approximately once per week during 1992. Nitrous oxide mixing ratios at the surface were also measured by CMDL (J. Butler, personal communication, 1995). Profiles of tropospheric methane and nitrous oxide were not available, so their mixing ratios from the surface to 10-15 km were set equal to the monthly average surface values. Their seasonal cycles were used to estimate the uncertainty in the mixing ratios in the troposphere, about 30 ppbv for methane and 1 ppbv for nitrous oxide. These uncertainty values were doubled between 10 and 15 km, where it was necessary to match the surface values to UARS data in some cases. Methane above 15 km was obtained from CLAES in January and May and HALOE in October. Concentrations of nitrous

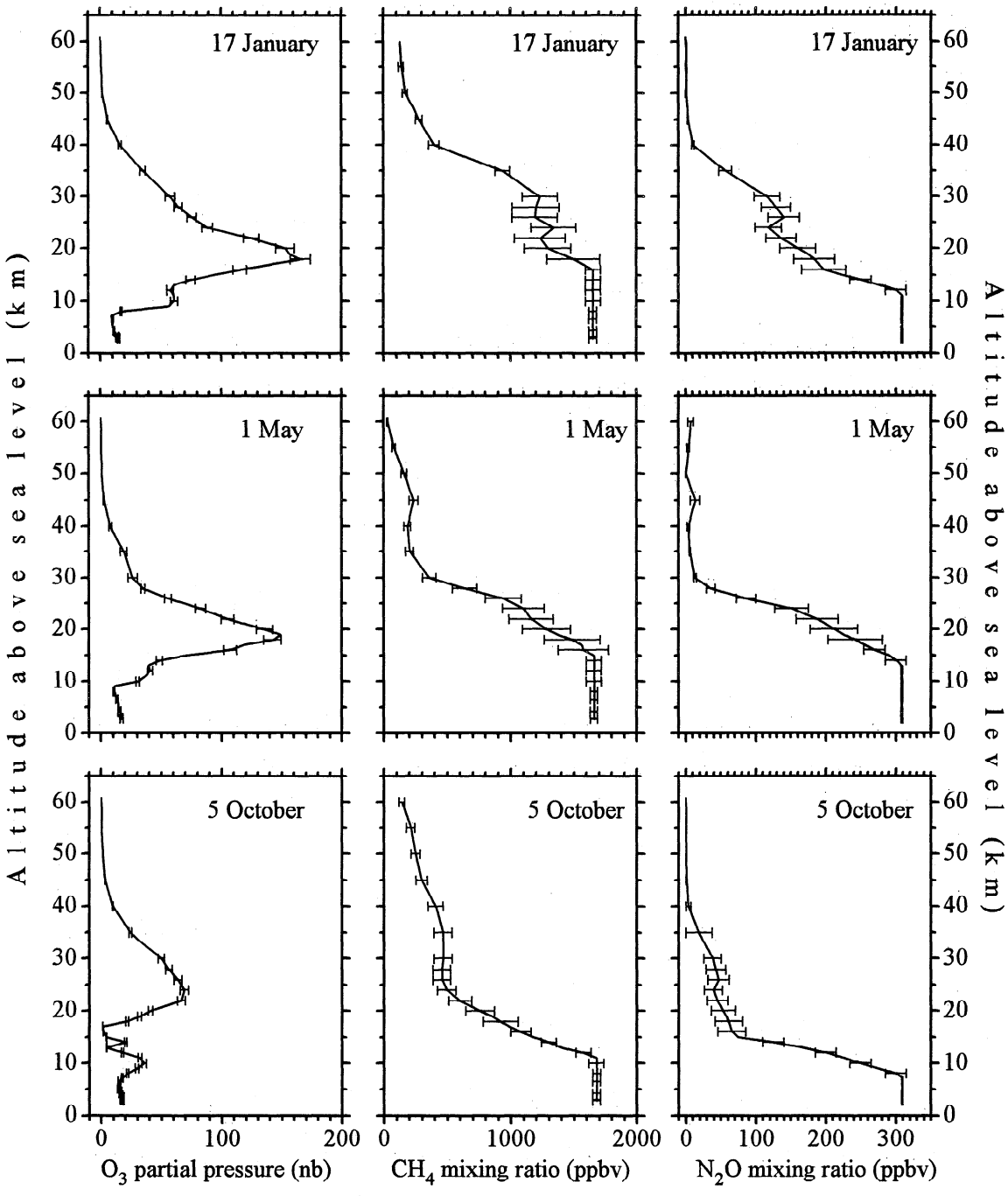

Figure 8. Vertical profiles of ozone, methane, and nitrous oxide for the three model atmospheres. Error bars are discussed in the text.

oxide for the January and May cases came from CLAES. Nitrous oxide data were not available for October 5, so the values above 15 km were set to one third the value of the CLAES data from January 17 in rough agreement with data from Figure 6 of *Randall et al.* [1994]. The estimated relative uncertainty for October 5 is double that of the January case. Figure 8 shows the vertical profiles of methane and nitrous oxide used in the model atmospheres.

The chlorofluorocarbons, CFC-11 and CFC-12, were included in a manner similar to that for CH_4 and N_2O. Their mixing ratios at the surface were measured by CMDL. The monthly average surface values were used up to about 15 km: about 266 pptv for CFC-11 and 495 pptv for CFC-12. Data from CLAES for January 17 were used above 15 km for all three test cases, since data were not available for May 1 and October 5. Sensitivity studies showed that the downward radiance is insensitive to the uncertainty in the stratospheric concentration but that it is important to specify the observed decrease in concentration above 15 km.

Oxygen was also included to account for its weak emission band from 1390 to 1760 cm^{-1}. Its mixing ratio was set to 20.95% by volume [*Goody and Yung*, 1989].

CCl_4 was not included because its contribution to emission at 790 cm^{-1} appears to be within the estimated radiance uncertainty. HNO_3 was not included because its tropospheric concentration was not measured at South Pole.

6. Radiative Transfer Calculations

6.1 Line-By-Line Radiative Transfer Model

This model (LBLRTM) was developed for the ARM program [*Clough et al.*, 1992] and has become a standard in the atmospheric radiation community. It is a vectorized version of FASCOD3 [*Clough et al.*, 1989b] and is used here to calculate radiance in a vertically inhomogeneous, but horizontally homogeneous, atmosphere. *Clough et al.* [1992] described the numerical techniques and approximations used to implement the radiative transfer equation in LBLRTM and also compared its output with another LBL model that was used in the ICRCCM study. LBLRTM has also been compared with accurate spectral radiance measurements taken at midlatitudes [*Clough et al.*, 1989a; 1992]. Example calculations were given by *Clough et al.* [1992] and *Clough and Iacono* [1995]. Version 3 of LBLRTM, released in April 1996, is employed here in conjunction with the 1992 version of the high-resolution line parameter (HITRAN) database [*Rothman et al.*, 1992].

The input to LBLRTM is provided by the model atmospheres described above. The specified wavenumber range in LBLRTM exceeds the bandwidth of the UD interferometer by at least 25 cm^{-1}. The zenith angle is set to the value of the angle readout given by UD's interferometer after being adjusted slightly for the measured tilt of the roof upon which the interferometer was mounted. The observation height specified within LBLRTM is 10 m above the surface, because the interferometer occupied a rooftop location 10 m above the surrounding snow surface. The maximum height and vertical resolution of the model atmospheres are specified below. All other values required by LBLRTM are set to the default values; in particular, the line shape calculation uses a Voigt profile that extends to 25 cm^{-1} from the line centers.

The water vapor continuum is represented by the Clough-Kneizys-Davies (CKD) model, version 2.2. *Clough et al.* [1992] showed the importance of including the self- and foreign-broadening effects of water vapor in a manner consistent with observations. They used the sub-Arctic winter standard atmosphere to illustrate the particular importance of the foreign continuum for cold atmospheres. The original CKD model [*Clough et al.*, 1989c] has been updated on the basis of comparisons with atmospheric spectral radiance data.

One advantage of using a model for calculating atmospheric radiances is that the full infrared spectrum can be examined, beyond the spectral limits of the measurements. Figure 9 shows radiance calculations for the three model atmospheres at a viewing zenith angle of 45° from 100 to 2000 cm^{-1} (5 to 100 μm). In Figure 9a the spectrum is labeled according to contributions from the major radiatively active gases. The radiance is lower in the winter (May 1) and early spring (October 5) than in summer (January 17), because of lower atmospheric temperatures.

The relatively transparent portion of the water vapor rotational band extends from the wing of the carbon dioxide band at 550 cm^{-1} to around 350 cm^{-1}. This spectral region is of particular importance to the radiative balance of polar atmospheres. The

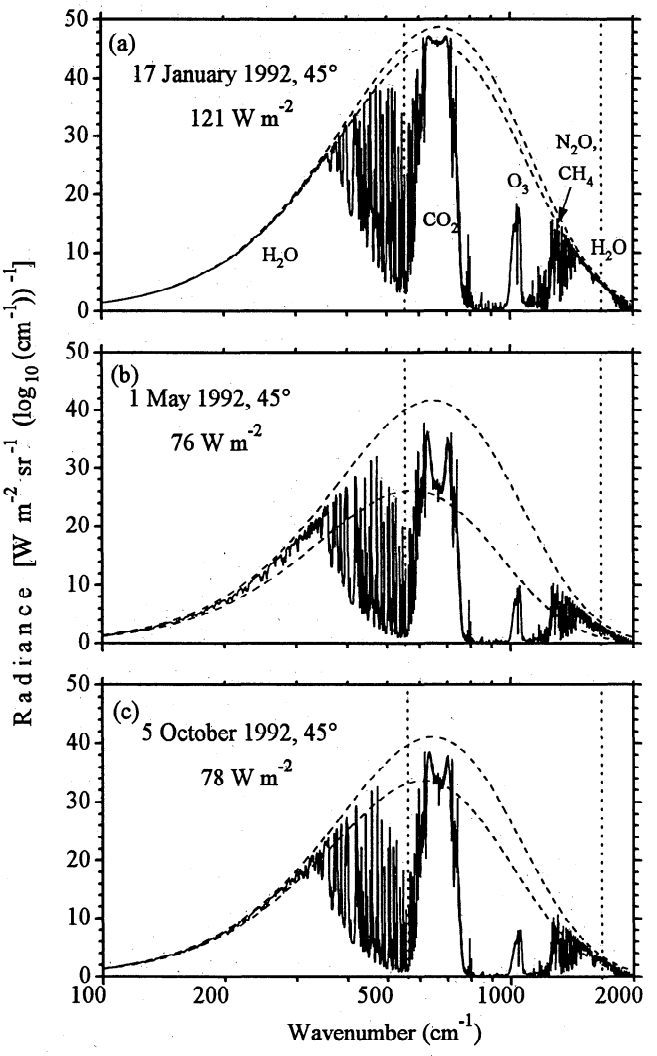

Figure 9. Radiance calculations for the three model atmospheres at a viewing zenith angle of 45° from 100 to 2000 cm^{-1} (5 to 100 μm). The vertical dotted lines represent the bandwidth of the measurements obtained by using the UD interferometer. The dashed curves are Planck radiances for the air temperatures at 21 m above the surface (lower curve) and the top of the inversion layer about 1.2 km above the surface (warmer; upper curve). Values are given in the figure for the total downward infrared flux at the surface; they were measured by a pyrgeometer.

emission from the water vapor rotational bands at $\nu < 350$ cm^{-1} matches a Planck curve well in summer, but not in the winter and spring because of the low water vapor amounts. This fact is somewhat true as well for the vibration-rotation band of water vapor at 1400 to 1600 cm^{-1}. Even though the atmosphere over the Antarctic Plateau contains at most only 1 mm of precipitable water, and thus emission from the water vapor continuum (between about 600 and 1000 cm^{-1}) is small, water vapor is still the primary emitter of thermal radiation to the surface [*Walden and Warren*, 1994], contributing about two thirds of the total downward flux to the surface. The 667-cm^{-1} (15-μm) absorption band of carbon dioxide is important because it is strong and is located near the peak of the Planck function. The near-surface temperature inversion is strongest in May and weakest in January; its effect on the carbon dioxide band is evident. Emission from ozone at 1042 cm^{-1} is maximum in January; it is lower in May because of low stratospheric temperatures, and even lower in October because of reduced ozone abundance. The emission bands of methane and nitrous oxide around 1100 to 1200 cm^{-1} are also visible. The N_2O band at 1168 cm^{-1} contributes in the window region, while emission from both CH_4 and N_2O overlaps with water vapor between 1200 and 1300 cm^{-1}. CH_4 and N_2O are therefore relatively more important in winter, when emission from water vapor is weaker.

The importance of the near-surface air temperature and the various atmospheric window regions is seen by comparing the Planck functions with the spectral radiance. Two Planck functions are plotted: one for the surface air temperature at 2 m and the other for the temperature at the top of the inversion. The peaks of the Planck functions for the January case are centered on the carbon dioxide band, whereas in May and October, when the temperatures are lower, the peaks are on the low-wavenumber side of the band. The carbon dioxide band is relatively more important to the surface energy budget in Antarctica than at other terrestrial locations both for this reason and also because emission from water vapor is small and therefore has little overlap with the CO_2 band.

The radiance values between the vertical dotted lines in Figure 9 constitute the standard model calculations used throughout this paper because this is the wavenumber region measured by the interferometer. The comparisons discussed below represent the most variable and perhaps most interesting portion of the infrared spectrum, but they do not provide a check on the emission from water vapor at low (<550 cm^{-1}) and high (>1667 cm^{-1}) wavenumbers.

6.2 Matching Calculations to Measurements

To compare spectral radiance observations with the results of a high-spectral-resolution radiative transfer model such as LBLRTM, it is necessary to account for the finite field of view (FOV) of the interferometer and also to match the spectral resolution of the calculations to that of the observations. *Steel* [1964] and *Bell* [1972] discuss such corrections in general terms. The discussions by *Clough et al.* [1989a] and *Smith et al.* [1989] apply this theory to comparisons of LBL calculations with interferometric measurements of atmospheric radiance and transmission. In this study, LBLRTM calculations are converted to spectra suitable for comparisons with observed spectral radiances by using the following procedure. LBLRTM calculates a spectrum at its own internal spectral resolution, which is about 0.001 cm^{-1}. An interferogram is generated from the calculated spectrum, then apodized by using the Hann-window function [*Press et al.*, 1992]. (This apodization function was also applied to the measured interferograms, and for proper comparisons it is necessary to apply the same apodization function to the calculations.) This interferogram is used to interpolate the spectrum to a wavenumber spacing of 0.01 cm^{-1}, much finer than the wavenumber grid of the transformed apodized interferogram. This procedure is all done within LBLRTM. The resulting calculated spectrum now matches the spectral resolution of the radiance measurements. A FOV correction [*Walden*, 1995] is applied by using trapezoidal integration to perform the integral over field of view,

$$L_{LBL}(\nu') = \int_0^1 \frac{w(\mu)}{\mu} L_a\left(\frac{\nu'}{\mu}\right) d\mu \qquad (10)$$

where L_a is the apodized version of the calculated spectrum. The variable of integration, μ, is the cosine of the angle θ measured from the center of the FOV. The outer limit of the FOV is at $\theta = \theta_m$. The weight $w(\mu)$ is set to the constant value of 1.0 from $\mu = 0.9996$ ($\theta_m = 1.5°$) to $\mu = 1$ and set to zero elsewhere. Sensitivity studies show that the calculated spectra described in this study are insensitive to reasonable assumptions about the shape of the FOV and uncertainty in the choice of θ_m. Finally, the oversampled, field-of-view-corrected, calculated spectrum is linearly interpolated from its fine wavenumber grid to the coarser grid of the measurements, allowing L_{LBL} to be directly compared to L_s from equation (2).

Before the correction was applied, there were large differences between the observed spectra and the LBLRTM calculations where the spectrum varied rapidly, notably in the wings of the CO_2 band near 600 and 750 cm^{-1}. The FOV correction greatly reduced these differences.

The radiances supplied to the ICRCCM project by *Walden et al.* [1997] differ slightly from those reported here in two ways. First, *Walden et al.* [1997] re-calibrated the radiance measurements by adjusting the temperatures of the calibration sources [$T_w - n*\sigma(T_w)$ and $T_c + n*\sigma(T_c)$], choosing a value of n as necessary to eliminate most of the negative radiances in the atmospheric window regions; n = +1 for Jan 17 (45°), 0 for Jan 17 (75°), +1 for May 1 (45°), 0 for May 1 (75°), +1 for Oct 5 (45°), +2 for Oct 5 (75°). Second, *Walden et al.* [1997] chose to remove the effect of the FOV from the measurements rather than incorporate it into the calculations. This was done by adjusting the wavenumber scale of the original measurements, ν, by $\nu' = \nu / (\cos\theta_m)$. This corrects for the wavenumber shift caused by off-axis rays in the interferometer, but does not account for the slight spectral smearing; both effects are described by *Bell* [1972].

7. Uncertainties in the Calculated Radiances

There are many possible sources of error in the LBLRTM calculations. These include uncertainties in the specification of the model atmosphere, the database of absorption line parameters (HITRAN92), the model's numerical techniques, and the treatment of the physics of infrared emission and absorption. *Ellingson et al.* [1991] briefly discussed the three latter sources, finding that LBL models agree well with each other where accurate spectroscopic data are available (e.g., carbon dioxide), indicating that the different numerical techniques used in the various models were all adequate. However, large uncertainties persist where there are deficiencies in the line parameter data, the theory of gaseous absorption, or the specification of the model atmosphere. The purpose of the following error analysis is to place a lower bound on the radiance error in the model calculations by considering only those sources of error induced by uncertainties in the specification of the model atmosphere and in the viewing zenith angle.

7.1 Maximum Height of the Model Atmosphere

The error in calculated radiance caused by truncating the model atmosphere is determined by subtracting the radiance for a 60-km atmosphere from those truncated at 30, 40, or 50 km. These radiance differences are negative, since the emission from a truncated atmosphere is less. The radiance errors for a 30-km atmosphere are significant, especially near the 1042-cm^{-1} ozone band, where they exceed -0.8 mW m^{-2} sr^{-1} $(cm^{-1})^{-1}$. The errors are seen primarily in spectral regions with weak absorption, where emission can come from throughout the atmosphere. The difference in radiance between a 50-km atmosphere and a 60-km atmosphere is very small (less than -0.02 mW m^{-2} sr^{-1} $(cm^{-1})^{-1}$), so we judge 60 km to be adequate and use this as the maximum height in all further calculations.

7.2 Vertical Resolution and Temperature Structure in the Lowest 300 m

Ideally, an altitude grid can be chosen that adequately represents the near-surface temperature inversion over the plateau in winter, when it is steepest. Model atmospheres with extreme inversions and large zenith angles are most sensitive to changes in the vertical resolution, so it is best to use such cases for choosing the vertical resolution. We chose the October 5 atmosphere at a zenith angle of 75°, since its temperature gradient in the lowest 100 m is the steepest of the three model atmospheres. Several different altitude grids between the surface (2.84 km) and 3.15 km are defined: grids with uniform spacings (10, 20, and 30 m) and a variable grid with spacing varying from 5 to 100 m, increasing with altitude. Between 3.15 and 60 km the grid spacing varies from 150 m to 5 km, gradually increasing with altitude, and is held constant in these sensitivity studies. The appropriate vertical resolution is chosen by successively decreasing the uniform altitude spacing in the near-surface layer until the radiance difference between successive runs is smaller than a specified tolerance. This tolerance is chosen as the radiance error induced by uncertainties in the temperature profile, discussed below.

The calculated radiance is sensitive to vertical resolution mainly in spectral regions that are strongly absorbed; i.e., regions in which most of the measured radiance originated in the inversion layer. The 30-m grid causes significant differences, but the 10-m and 20-m grids give almost identical results. Both still show a difference from the variable grid in the CO_2 band, but this difference is small in comparison with radiance errors caused by the uncertainty in the specification of the temperature profile, discussed next. The calculations shown below use the variable grid.

7.3 Radiance Error Due to Uncertainty in Atmospheric Temperature and Composition

With the vertical resolution and the height of the model atmosphere chosen so that they induce little error in the LBLRTM calculations, the radiance error is now determined by performing sensitivity studies by using the model atmosphere data and their uncertainties. Standard spectral radiance calculations are produced using the profile information presented in Figures 7 and 8. Radiance errors are determined by perturbing, one at a time, an individual profile in the model atmosphere by adding its uncertainty. LBLRTM is then run with this perturbed model atmosphere, yielding a radiance spectrum. The radiance errors are found by subtracting the standard radiance case from that obtained with the perturbed atmosphere. The total radiance error is found by taking the square root of the sum of the squares of the radiance differences due to the various profile perturbations.

The results for January 17 at 45° and May 1 at 75°, representing the warmest and coldest atmospheres at South Pole, are shown in Figure 10. These radiance errors represent the range of errors to be expected for clear-sky calculations with LBLRTM for the Antarctic Plateau. Only the four major sources of error are shown in Figure 10; the errors due to uncertainty in concentrations of carbon dioxide, methane, nitrous oxide, CFC-11, and CFC-12 are all negligible in comparison with those shown. The radiance errors for October 5 are similar to those for May 1. The total radiance error in summer is dominated by uncertainties in the temperature and water vapor profiles. In winter the uncertainty in zenith angle (discussed below) is also a major contributor. The total error in calculated radiance for these cases is comparable to the error in measured radiance shown in Figure 6. However, the spectral structure is different. It should be emphasized that the error estimates for the LBLRTM calculations assume the sky is clear. The visual sky observations were initially used to identify clear test cases, but subvisible clouds and aerosols may still have been present in the actual atmosphere. This possibility is examined below.

The uncertainty in zenith angle is due to many sources, some of which are quantified here and some of which are estimated. The angle readout for the interferometer's mirror assembly was accurate to within a few millivolts, or roughly 0.1°. The tilt of the roof during 1992 was estimated as 0.4° ± 0.1°. Additional sources of uncertainty included the interferometer being mounted in a nonlevel position and inaccuracy in calibration of the angle readout (which is ideally set to 0° when viewing vertically and 90° when viewing horizontally). One test indicated that the zenith angle was actually 73.8° at the 75° mechanical mirror stop, an offset of 1.2° if it is assumed that the angle readout was set to exactly the 75° voltage during that test (R. Van Allen, personal communication, 1995). When all these sources of uncertainty are taken into account, a generous estimate of the overall zenith angle uncertainty is ±1.5°.

The radiance errors induced by the uncertainty in the zenith angle are most significant in the wintertime. The largest contributions are primarily in regions where gases have intermediate absorption, i.e., the wings of the carbon dioxide band, the weak bands of carbon dioxide (975 cm^{-1}) and nitrous oxide (1168 cm^{-1}), the ozone band, and methane, nitrous oxide, and water between 1200 and 1500 cm^{-1}. Emission from these regions comes from a long path length in the atmosphere and therefore comes on average from a great distance from the observation point. The farther away the emission region, the greater the change in effective emitting temperature due to a given change in zenith angle (if the temperature varies with height). The radiance error is large in the ozone band because most ozone emission comes from the upper troposphere and lower stratosphere. The zenith angle uncertainty induces much less error in summer because of weaker temperature gradients; the error is confined to the wings of the carbon dioxide band.

The uncertainty in the temperature profile produces radiance errors in spectral regions where emission is from altitudes at which the temperature is changing rapidly and where gases are strongly absorbing. Most of the errors in both summer and winter are from emission within the inversion layer (carbon dioxide and water vapor), but there is also a significant contribution in the ozone band.

The radiance errors due to water vapor and ozone are confined to regions in which they emit radiation. The errors are largest where the uncertainty in the individual profile is greatest. Thus, for water vapor, the errors occur in spectral regions where emis-

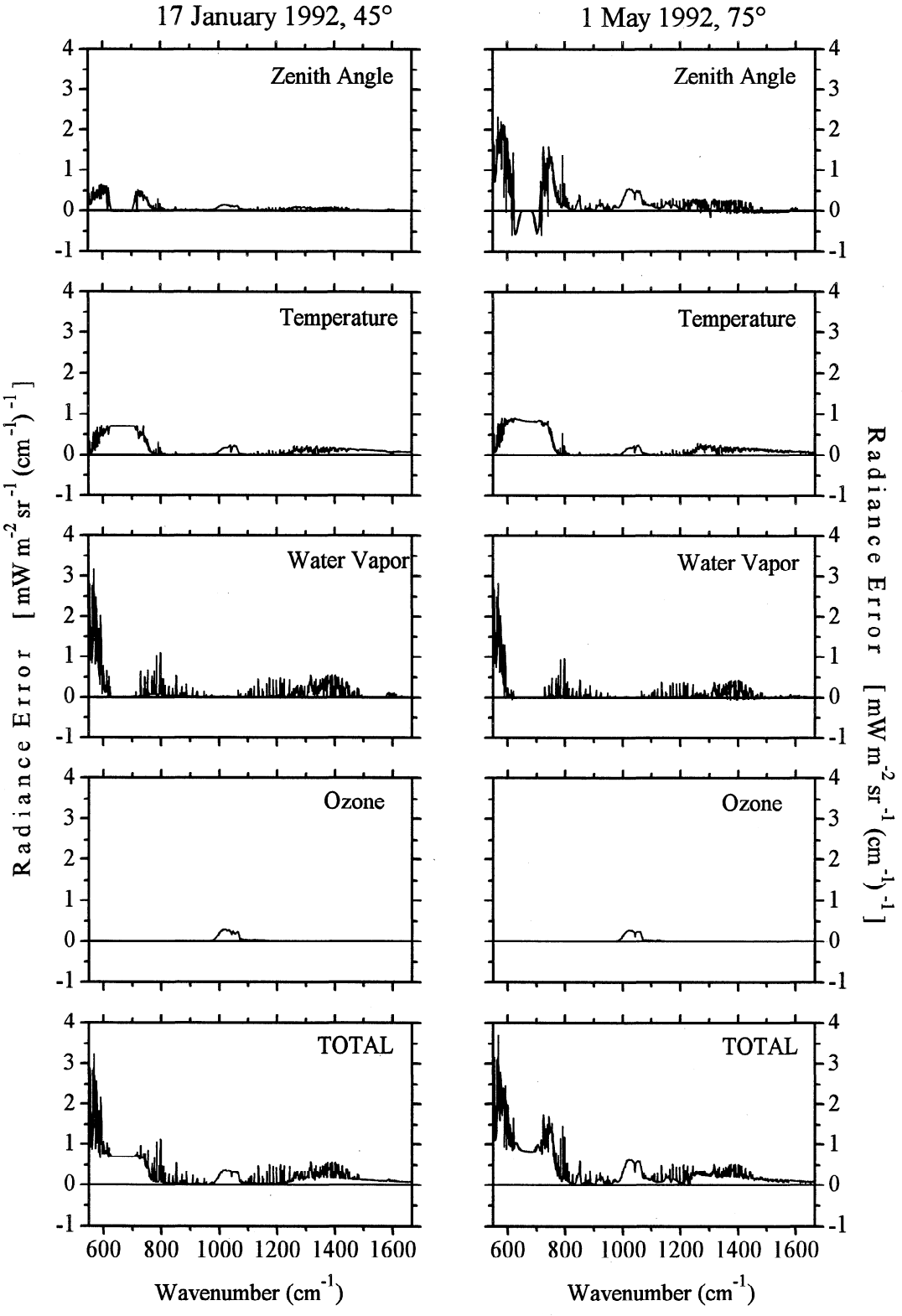

Figure 10. Estimated radiance errors for January 17, 1992, at 45° and May 1, 1992, at 75° based on sensitivity studies using the model atmospheres. The total error is the quadrature sum of the radiance errors induced by the various profile perturbations discussed in the text. The wavenumber range corresponds to the bandwidth of the UD interferometer.

sion is from the free troposphere and stratosphere (above 4 km); i.e., regions of intermediate and weak absorption. LBLRTM is insensitive to changes in water vapor from 625 to 700 cm^{-1} because of overlap with carbon dioxide. The errors between 550 and 600 cm^{-1} are large because the Planck function peaks near these wavenumbers and the tropospheric water vapor amounts are quite uncertain. The radiance errors due to uncertainties in ozone concentration are confined to the 1042-cm^{-1} band.

8. Spectral Radiance Comparisons

The measurement and calculation for May 1 at 75° are shown in Figure 11 along with their difference. This case is used for further discussion below, since it is the most extreme model atmosphere in terms of low surface temperature (-66°C), strength of the surface-based temperature inversion (30 K), and low temperatures throughout the atmosphere. Figure 12 shows the radiance differences for all six cases.

The overall agreement between the observations and LBLRTM is good. In absolute radiance, differences are comparable to those reported from SPECTRE [*Ellingson and Wiscombe*, 1996]. We judge radiance differences to be significant, and requiring explanation, if they exceed twice the estimated combined radiance error from both the measurements and calculations. This situation occurs only in a few spectral regions, discussed below along with a general discussion of the overall comparisons in the following spectral bands: carbon dioxide (550-800 cm^{-1}), 11-μm window (800-990 cm^{-1}), ozone (990-1070 cm^{-1}), 9-μm window (1070-1200 cm^{-1}), methane and nitrous oxide (1200-1350 cm^{-1}), and water vapor (1350-1500 cm^{-1} and 1500-1667 cm^{-1}). Selected portions of the spectra for May 1 at 75° are plotted in Figure 13 along with the radiance difference and the estimated error in the radiance difference. The error in radiance difference is the square root of the sum of the squares of errors in the measurements and calculations.

8.1 Carbon Dioxide

In the carbon dioxide band from 550 to 800 cm^{-1} (Figures 11 and 12) the agreement is fairly good in all cases. The spurious line at 667 cm^{-1} often seen in the measurements and in the radiance differences is due to very strong absorption by carbon dioxide where the instrument mostly views its internal temperature. At this frequency the ratio of the difference spectra, γ, is indeterminate; see equations (2) and (3). The spectral structure in the radiance differences between 600 and 725 cm^{-1}, particularly in May and October when the temperature gradient is large, is probably due to error in specification of the temperature structure and zenith angle. The largest differences in this band are between 550 and 600 cm^{-1}, shown in Figure 13a. This figure shows that the spectral details in the measurements and calculations agree quite well, giving confidence in the field of view correction and the spectral resolution correction, and indicating that the signal-to-noise ratio is adequate at this end of the interferometer's bandwidth, where the instrument response is dropping rapidly. The large offset between 570 and 600 cm^{-1} points to a consistent problem in the winter when the calculation is usually larger than the measurement. It is possible that the uncertainty in the calibration source emissivity has been underestimated in this spectral region (see Figure 4). This possibility precludes detection of faults in the radiative transfer model or the spectroscopic data in this spectral region.

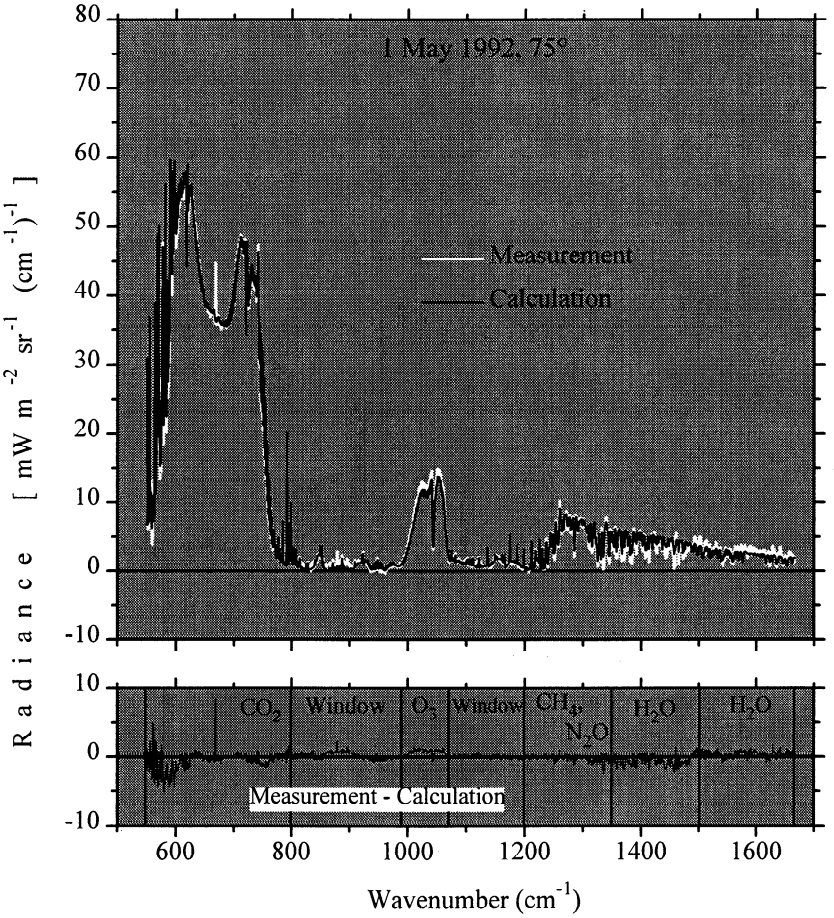

Figure 11. Spectral radiance measured by the UD interferometer, compared with LBLRTM calculations for May 1, 1992, at 75°. The lower frame is the radiance difference on the same scale, where the primary infrared emitters in each spectral band are also indicated.

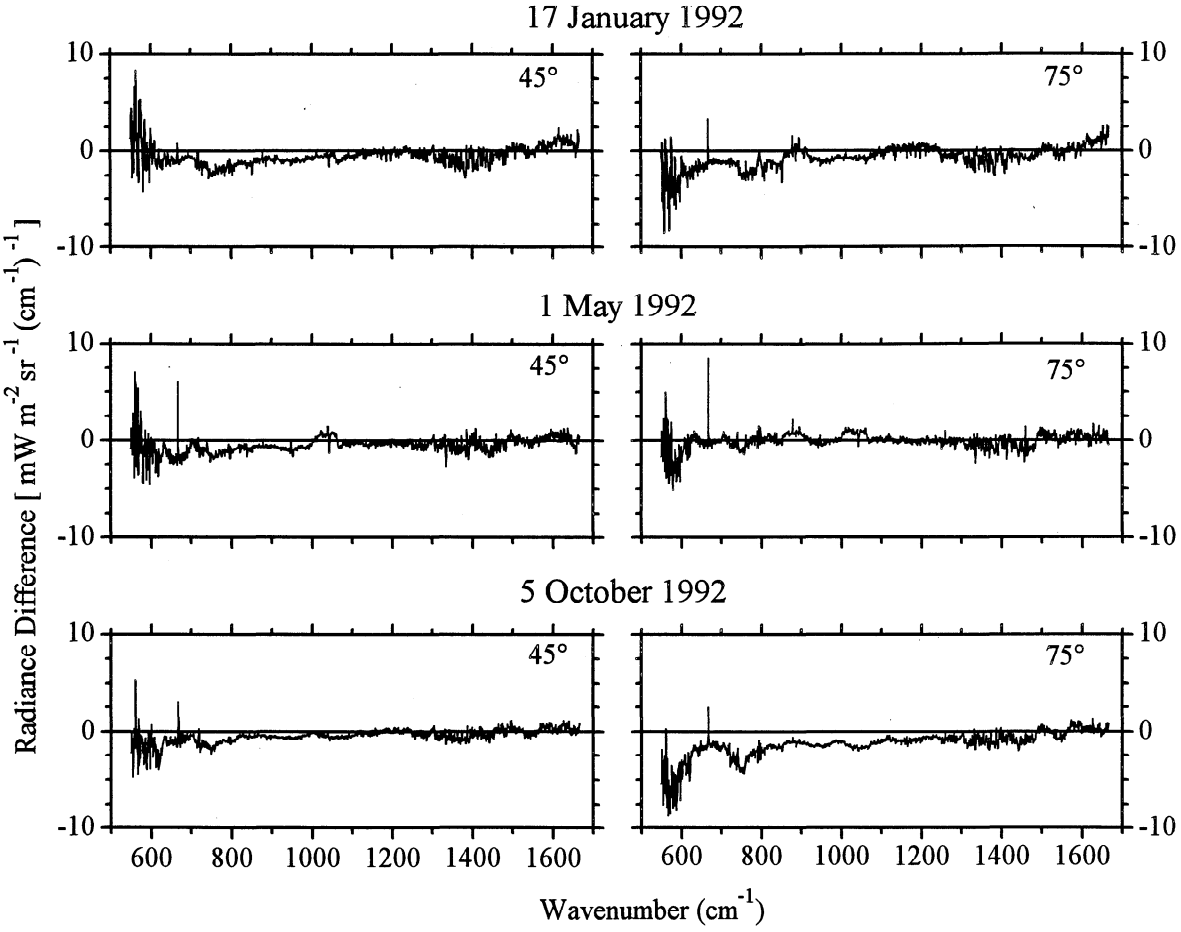

Figure 12. Spectral radiance comparison of LBLRTM calculation with interferometer measurement for the six test cases. The comparisons are shown as radiance differences, measurement minus calculation. The May 1, 1992 case at 75° is the same as the radiance difference shown in Figure 11.

8.2 The 11-μm Window

The window region is the most transparent portion of the interferometer's bandwidth, and therefore emission from clouds, aerosols, and diamond dust ice crystals are easily detected here. The sky observation for May 1 indicated the presence of diamond dust ice crystals, which is typical for clear skies in winter at South Pole. On October 5, PSCs may have been present over South Pole, since the temperature near 15 km (-81°C; Figure 7) was below the threshold (195 K or -78°C) at which they are expected to form. Ice crystals and clouds, if present, would cause the measured radiance to exceed the clear-sky calculation, which would give a positive radiance difference (measurement minus calculation). However, the radiance differences plotted in Figures 11 and 12 (and on an expanded scale in Figure 13b) are both positive and negative and not significantly different from zero in this spectral region, suggesting that they are not due to the presence of ice crystals or PSCs. This result is particularly evident in the January and October cases where the calculated radiance exceeds the measured radiance. Since no significant negative radiance differences exist in any of the comparisons, the emission from diamond dust ice crystals and PSCs, if present, is within the estimated error.

In Figure 13b, emissions from CFC-11 and CFC-12 are apparent, as well as water vapor lines. The weak absorption band of carbon dioxide is visible around 960 cm^{-1}. The radiance difference between 850 and 900 cm^{-1} is on average larger than other regions in Figure 13b because nitric acid was not included in the LBLRTM calculation.

8.3 Ozone

Ozone emission is seen in Figure 13c. The spectral details correspond well, validating both the HITRAN spectral line parameter data and the FOV and spectral resolution corrections applied to the calculations. The differences seen in Figure 13c are within twice the estimated radiance error. The six comparisons (Figure 12) show no consistent bias in the calculations in relation to the measurements and therefore suggest possible errors in the individual ozone profiles.

8.4 The 9-μm Window

Ozone and nitrous oxide (1168 cm^{-1}) exhibit weak emission between 1070 and 1200 cm^{-1}, as Figure 13d shows. These Antarctic spectra are ideal for viewing these features, since elsewhere on Earth they are obscured by the water vapor continuum. The radiance differences are generally within the estimated errors.

8.5 Methane and Nitrous Oxide

In the portion of the spectrum where nitrous oxide, methane, and water vapor overlap (1200-1350 cm^{-1}) there is good agreement (Figure 13e). The spectral details seen in both the observa-

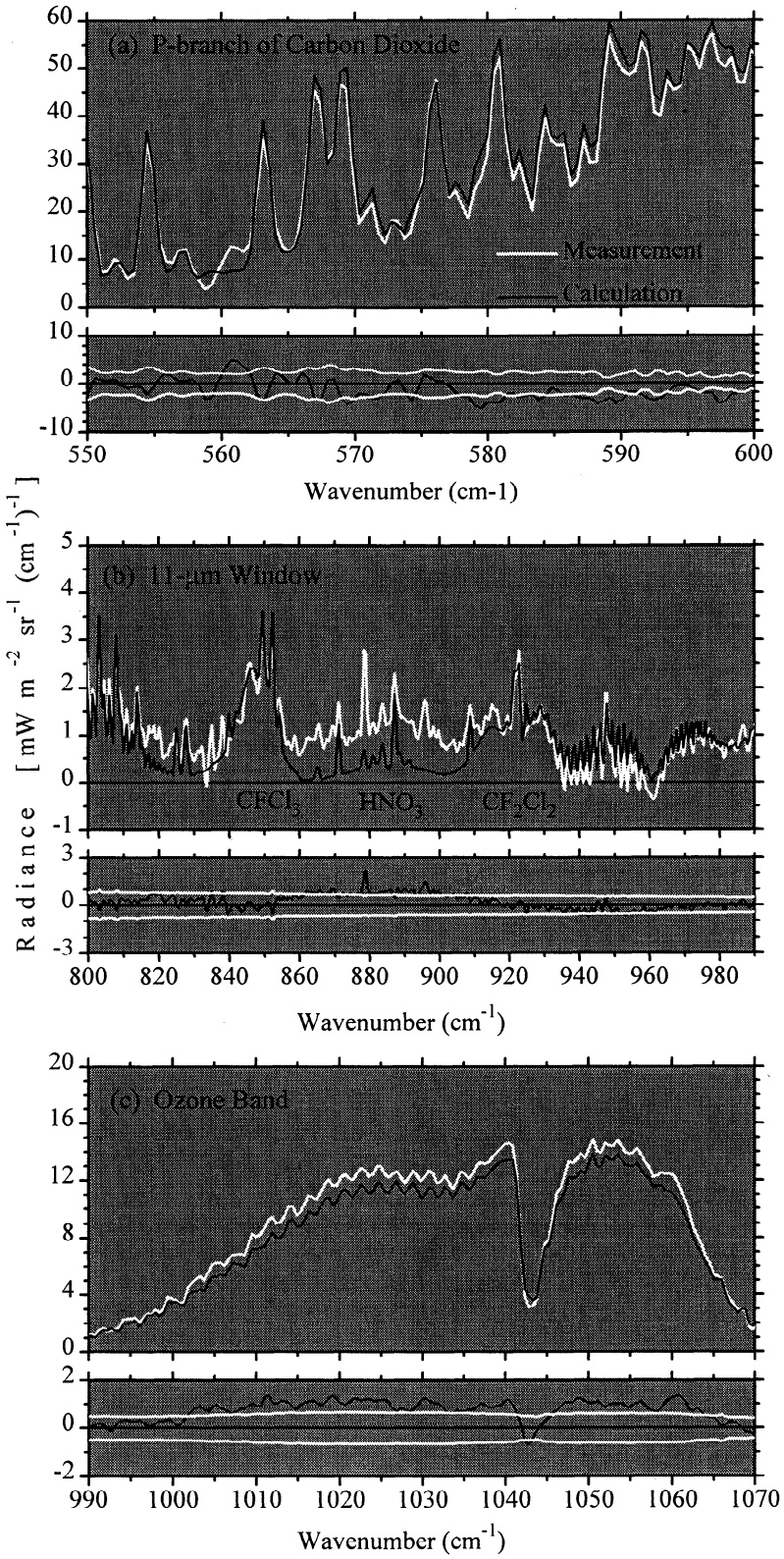

Figure 13. Radiance comparisons for May 1, 1992, at 75°. (top) Spectral radiance measured by the DU interferometer plotted with the corresponding LBLRTM calculation; (bottom) Expanded vertical scale of the radiance difference (measurement minus calculation) together with the positive and negative values of the estimated uncertainty in the radiance difference. Each frame displays a different spectral region. Both the horizontal and vertical scales differ from one frame to the next. (a) 550-600 cm^{-1}. The approximate flux F in this band is 4.8 W m^{-2}; the approximate flux difference (measurement minus calculation) ΔF is -0.2 W m^{-2}. (b) 800-990 cm^{-1}. F = 0.5 W m^{-2}; ΔF = +0.1 W m^{-2}. (c) 990-1070 cm^{-1}. F = 2.1 W m^{-2}; ΔF = +0.2 W m^{-2}. (d) 1070-1200 cm^{-1}. F = 0.5 W m^{-2}; ΔF = 0.0 W m^{-2}. (e) 1200-1350 cm^{-1}. F = 2.1 W m^{-2}; ΔF = -0.1 W m^{-2}. (f) 1350-1500 cm^{-1}. F = 2.0 W m^{-2}; ΔF = -0.2 W m^{-2}.

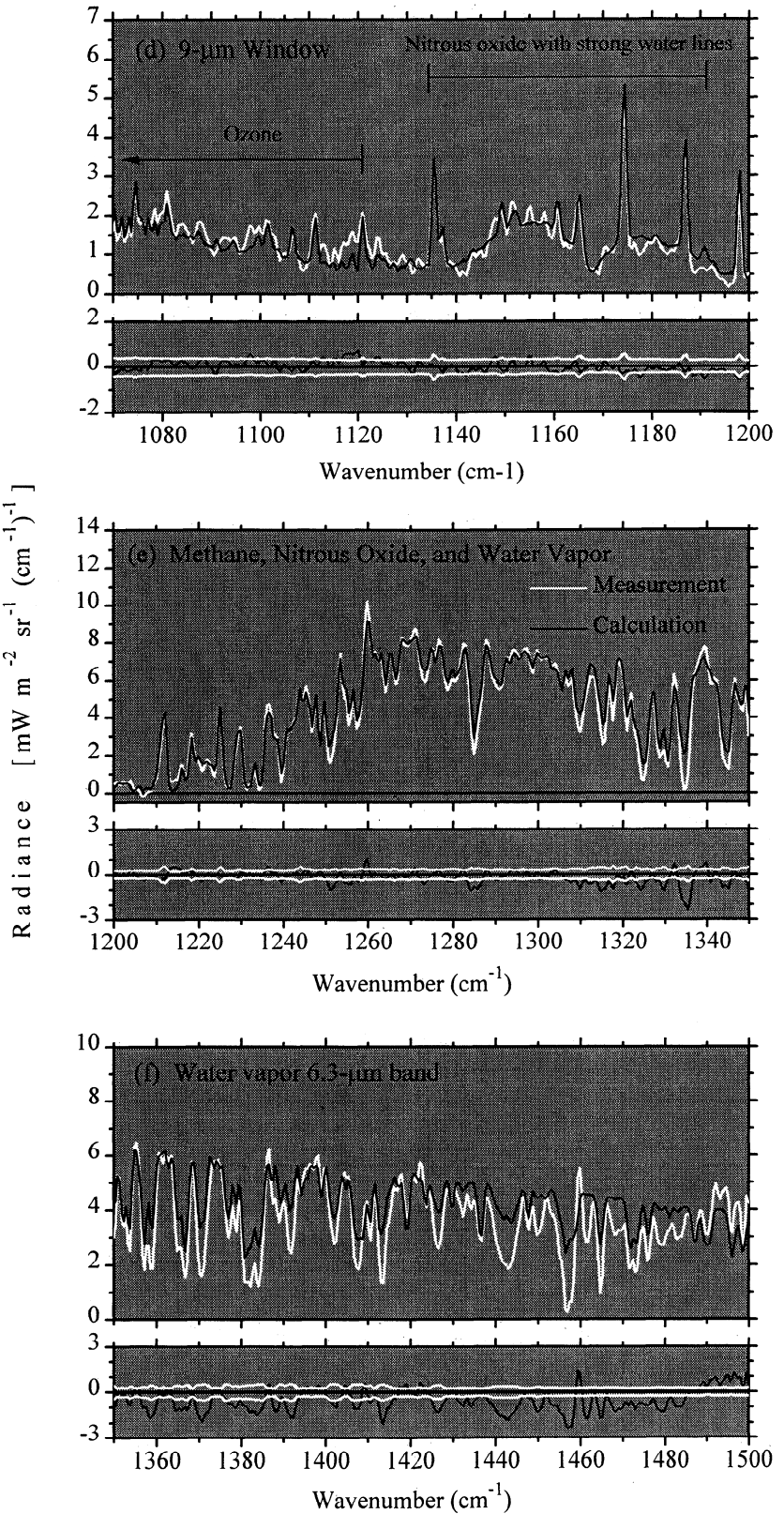

Figure 13. (continued)

tions and LBLRTM calculations are similar. The comparisons are quite good between 1200 and 1250 cm^{-1}, even at low radiance levels. However, there is a tendency for the calculated radiances to exceed the measurements between spectral lines in the region 1250-1350 cm^{-1}.

8.6 Water Vapor

The tendency for calculations to exceed measurements between spectral lines is more pronounced from 1350 to 1500 cm^{-1} (Figure 13f), where emission is primarily due to water vapor. In general, the peaks of spectral lines agree well, but there are large offsets

between lines with, in some cases, striking similarities in spectral detail (for instance, around 1380 cm^{-1}). Figure 12 shows the calculation generally exceeding the radiance observation (negative radiance differences) from 1250 to 1500 cm^{-1} for all six cases, especially between strong water vapor emission lines. The radiance differences exceed twice the estimated error in all the model atmospheres, regardless of whether the residual calibration bias seen in the measured window radiances is positive or negative.

Sensitivity studies were performed on both the interferometric calibration and the radiative transfer calculations in an attempt to identify the cause of the discrepancies between 1250 and 1500 cm^{-1}. First, the temperature of the warm calibration source was adjusted to achieve better agreement in this spectral region, assuming the LBLRTM calculations were correct. The low values of the measured radiance between spectral lines are more sensitive to the calibration source radiance than are the peaks of the spectral lines. Thus it is possible to fit the measured spectrum to the radiance calculation by changing the warm source temperature. The warm source temperature was chosen as a proxy for changes in the calibration source radiance, since it is typically the largest source of uncertainty in the measured radiances. To minimize the spectrally averaged difference in radiance in this band, the warm source temperature had to be decreased by about 6 K. This adjustment provided a better match of the low radiances shown in Figure 13f, but it also increased unrealistically the radiance in other parts of the spectrum, particularly the window regions. Furthermore, a decrease in the warm source temperature of this magnitude would imply that the interferometer was viewing a source colder than that reported by the warm source thermistors, contrary to the evidence from three different tests shown in Appendix A of *Walden* [1995] and summarized in Figure 3b. Therefore miscalibration of the measured radiances cannot explain all of the radiance differences between 1250 and 1500 cm^{-1}.

Second, sensitivity studies with LBLRTM were performed by using different humidity profiles from the surface (2.8 km) to 7 km above sea level. As discussed above, the uncertainty in the water vapor profiles is large. The calculated spectra are most sensitive to humidity changes below 7 km, since most of the water vapor is contained in the troposphere. The low radiance values between spectral lines from 1250 to 1500 cm^{-1} are more sensitive to humidity changes than are the peaks of lines, because the peaks are saturated. Therefore the tropospheric humidity can be adjusted to fit the radiance calculation to the measured spectrum. As trial values, the tropospheric relative humidity with respect to ice (RH_i) was set to 25%, 50%, 75%, and 100%. As RH_i decreases from 100% to 50%, the discrepancies between the calculations and measurements also decrease. However, at RH_i = 25% the peaks of the spectral lines become subsaturated, and the agreement worsens. Therefore good agreement in both the peaks and valleys was impossible, but the best agreement was attained for tropospheric RH_i values of 25-50%. These low humidity values seem unreasonable, since ice crystal precipitation was observed on every clear day in winter and on most clear days in summer; the presence of precipitation implies saturated conditions somewhere within the lower atmosphere.

Clough et al. [1992] and *Thériault et al.* [1994] showed the importance of the foreign-broadened water vapor continuum in this spectral region, particularly in cold atmospheres where the continuum increases the opacity between spectral lines. The oxygen continuum is also important in cold and dry atmospheres from 1400 cm^{-1} to beyond the high-wavenumber limit of the interferometer [*Timofeyev and Tonkov*, 1978; *Rinsland et al.*, 1989]. *Revercomb et al.* [1990] and *Thériault et al.* [1994] found that calculations using FASCODE (the predecessor of LBLRTM) and an earlier version of the water vapor continuum model exceeded their measurements, as we also find. *Thériault et al.* [1994] calculated radiance along horizontal paths at temperatures of -8°C to +4°C and water vapor amounts of 0.6 to 1.2 g cm^{-2}. They suggested that perhaps either the foreign-broadened absorption coefficient has a positive temperature dependence or the temperature dependence of the strengths of nearby water vapor lines is in error. The foreign continuum absorption in the CKD model used here has a slight temperature dependence through density, but the continuum coefficients themselves do not depend on temperature (S. A. Clough, personal communication, 1995).

The final spectral region considered here (1500-1667 cm^{-1}) shows significant radiance differences (Figures 11 and 12), especially in January. This finding is surprising, since most of this spectral region is strongly absorbed by water vapor and thus should resemble a Planck curve, especially in January when the lowest 2 km are nearly isothermal. Sensitivity studies show that the choice of emissivity for the calibration sources has little effect on the comparisons. It is possible that the noise equivalent spectral radiance (Figure 6) was underestimated at these wavenumbers. However, since the errors are largest in January and appear to be a bias rather than noise, the radiance differences may be due to slight water vapor variations within the warm and relatively moist instrument during the measurement sequence that are not accounted for in the calibration process. Errors of this type would be most prevalent in spectral regions characterized by strong absorption and emission, e.g., beyond 1500 cm^{-1}.

9. Conclusions

A data set of downward longwave spectral radiance, measured at South Pole Station in 1992, is augmented with ancillary data to describe the atmosphere. An error analysis shows that the primary source of uncertainty in the spectral radiances is the temperature of the warm calibration source; uncertainty in its emissivity also contributes significantly. The overall measurement error is largest in spectral regions that are relatively transparent, particularly the atmospheric window region (800-1250 cm^{-1}). Three well-calibrated test cases are selected for clear-sky conditions.

The state of the atmosphere at the times of the test cases is constructed from radiosondes, water vapor sondes, and ozonesondes and from surface measurements of carbon dioxide, methane, nitrous oxide, CFC-11, and CFC-12 made at South Pole. Data from the UARS satellite are used to describe the upper atmosphere. Three model atmospheres have been constructed, including estimated uncertainties in all profiles. These data represent the coldest and driest test cases for radiative transfer models for terrestrial conditions.

The line-by-line radiative transfer model LBLRTM was used to calculate spectral radiances, using the ancillary data as input. Before the measurements were compared, the calculations were adjusted for instrumental effects, namely, the spectral resolution of the instrument and its finite field of view. Sources of error in the calculations have been estimated; they are induced by uncertainties in the viewing zenith angle and in the profiles of temperature and the principal radiatively active gases. The major contributors to this error are the uncertainties in the temperature and water vapor profiles. The uncertainty in the viewing zenith angle becomes important in winter, when a steep near-surface temperature inversion persists over the Antarctic Plateau.

The differences in radiance between the measurements and calculations are generally within twice the combined error in the measurements and calculations. However, discrepancies exist at both ends of the interferometer's bandwidth. Another region of discrepancy is between spectral lines from 1250 to 1500 cm^{-1}, where emission is from the foreign-broadened water vapor continuum. Sensitivity studies show that the discrepancies are probably not solely due to errors in the spectral radiance calibration or to inaccurate specification of the water vapor profiles and therefore suggest errors in either the spectroscopic database or the model of the foreign water vapor continuum, or both. Future field measurements in the polar regions should concentrate on accurately determining temperature and water vapor within the boundary layer. In addition, spectral radiance observations should be extended to wavenumbers as low as 300 cm^{-1} to fully measure the unsaturated portion of the water vapor rotational band. These suggestions apply in particular to the ARM site on the north slope of Alaska and to the Surface Heat Budget of the Arctic Ocean (SHEBA) experiment [*Moritz and Perovich*, 1996].

The spectral radiance measurements and their corresponding model atmospheres are available to the modeling community through ICRCCM [*Walden et al.*, 1997].

Acknowledgments. We thank Renate Van Allen and John Van Allen of the University of Denver for preparing their interferometer so that it met our needs at South Pole. Kathryn Price helped maintain the interferometer from November 1992 through January 1993. Henry Revercomb provided a reference calibration blackbody, manufactured by his group at the University of Wisconsin. We had many helpful discussions about interferometry with Gary Hansen (University of Hawaii), Robert Knuteson (University of Wisconsin), Jeff Peterson (Carnegie Mellon University), Henry Revercomb, and Renate Van Allen. Kitt Hughes, Bob Koney, B. K. Grant, and Peggy Klinedinst of the South Pole Weather Office provided us with radiosonde data and helped us characterize the response time of the radiosonde's thermistor. We thank Mike O'Neill and John Lowell of NOAA-CMDL for coordinating their launches of water vapor sondes with our interferometer measurements during 1990-1991, and Dale Tysor and David Gaines (also of NOAA-CMDL) for launching ozonesondes and water vapor sondes during 1992. Denise Worthen (University of Washington) measured the tilt of the Skylab roof. We had helpful discussions with R. O. Knuteson regarding field-of-view corrections. S. A. Clough and P. Brown of Atmospheric Environmental Research, Inc., supplied us with the radiative transfer model, LBLRTM, and answered our questions about how to use it with model atmospheres from the Antarctic. S. A. Clough also provided many helpful comments through his review. We acknowledge the Carbon Cycle, Acquisition and Data Management, and Nitrous Oxide and Halocompounds divisions of NOAA-CMDL for providing data. We acknowledge the South Pole Station crews of 1990-1991 and 1991-1992 for their help with our experiments. We thank the Upper Atmosphere Research Satellite (UARS) project (code 916), and the Distributed Active Archive Center (code 902.2) at the Goddard Space Flight Center, Greenbelt, Maryland, for the production and distribution of the UARS data, respectively. Their activities are sponsored by NASA's Mission to Planet Earth Program. This research was supported by NSF grants DPP-88-18570, OPP-91-20380, and OPP-94-21096.

References

Beer, R., *Remote Sensing by Fourier Transform Spectroscopy*, John Wiley, New York, 1992.

Bell, R.J., *Introductory Fourier Transform Spectroscopy*, 382 pp., Academic, San Diego, Calif., 1972.

Cacciani, M., P. di Girolamo, A. di Sarra, G. Fiocco, and D. Fuà, Volcanic aerosol layers observed by lidar at South Pole, September 1991 - June 1992, *Geophys. Res. Lett.*, *20*, 807-810, 1993.

Carroll, J.J., Long-term means and short-term variability of the surface energy balance components at the South Pole, *J. Geophys. Res.*, *87*, 4277-4286, 1982.

Clough, S.A., and M.J. Iacono, Calculations of atmospheric fluxes and cooling rates, 2, Application to carbon dioxide, ozone, methane, nitrous oxide, and the halocarbons, *J. Geophys. Res.*, *100*, 16,519-16,535, 1995.

Clough, S.A, R.D. Worsham, W.L. Smith, H.E. Revercomb, R.O. Knuteson, G.P. Anderson, M.L. Hoke, and F.X. Kneizys, Validation of FASCODE calculations with HIS spectral radiance measurements, in *IRS '88: Current Problems in Atmospheric Radiation* edited by J. Lenoble and J.F. Geleyn, pp. 376-279, A. Deepak, Hampton, Va., 1989a.

Clough, S.A., F.X. Kneizys, E.P. Shettle, and G.P. Anderson, FASCOD3: Spectral simulation, in *IRS '88: Current Problems in Atmospheric Radiation*, edited by J. Lenoble and J.F. Geleyn, pp. 372-375, A. Deepak, Hampton, Va., 1989b.

Clough, S.A., F. X. Kneizys, and R.W. Davies, Line shape and the water vapor continuum, *Atmos. Res.*, *23*, 229-241, 1989c.

Clough, S.A., M.J. Iacono, and J.L. Moncet, Line-by-line calculations of atmospheric fluxes and cooling rates: Application to water vapor, *J. Geophys. Res.*, *97*, 15,761-15,785, 1992.

Ellingson, R.G., and Y. Fouquart, The intercomparison of radiation codes used in climate models: An overview, *J. Geophys. Res.*, *96*, 8925-8927, 1991.

Ellingson, R.G., and W.J. Wiscombe, The spectral radiance experiment (SPECTRE): Project description and sample results. *Bull. Am. Meteorol. Soc.*, *77*, 1967-1985, 1996.

Ellingson, R.G., J. Ellis, and S. Fels, The intercomparison of radiation codes used in climate models: Long wave results, *J. Geophys. Res.*, *96*, 8929-8953, 1991.

Ellingson, R.G., S. Shen, and J. Warner, Calibration of radiation codes used in climate models: Comparison of clear-sky calculations with observations from the Spectral Radiance Experiment and the Atmospheric Radiation Measurement program, in *Proceedings of the Fourth Atmospheric Radiation Measurement (ARM) Science Team Meeting, 28 February - 3 March 1994, Charleston, South Carolina, DOE CONF-940277*, 47-53, 1995.

Fouquart, Y., B. Bonnel, and V. Ramaswamy, Intercomparing shortwave radiation codes for climate studies, *J. Geophys. Res.*, *96*, 8955-8968, 1991.

Genthon, C., Antarctic climate modeling with general circulation models of the atmosphere, *J. Geophys. Res.*, *99*, 12,953-12,961, 1994.

Goody, R.M., and Y.L. Yung, *Atmospheric Radiation, Theoretical Basis*, 2nd ed., Oxford Univ. Press, New York, 1989.

Hanson, K.J., Radiation measurement on the Antarctic snowfield: A preliminary report, *J. Geophys. Res.*, *65*, 935-946, 1960.

Hanson, K.J., and M.J. Rubin, Heat exchange at the snow-air interface at the South Pole, *J. Geophys. Res.*, *67*, 3415-3424, 1962.

Hervig, M.E., J.M. Russell III, L.L. Gordley, J. Daniels, S.R. Drayson, and J.H. Park, Aerosol effects and corrections in the Halogen Occultation Experiment, *J. Geophys. Res.*, *100*, 1067-79, 1995.

Komhyr, W.D., L.S. Waterman, and W.R. Taylor, Semiautomatic nondispersive infrared analyzer apparatus for CO_2 air sample analyses, *J. Geophys. Res.*, *88*, 1315-1322, 1983.

Komhyr, W.D., R.H. Gammon, T.B. Harris, L.S. Waterman, T.J. Conway, W.R. Taylor, and K.W. Thoning, Global atmospheric CO_2 distribution and variations from 1968-1982 NOAA/GMCC CO_2 flask sample data, *J. Geophys. Res.*, *90*, 5567-5596, 1985.

Kopanev, I.D., The heat balance of the Antarctic continent, in *Polar Meteorology, Tech. Note 87*, pp. 189-195, World Meteorol. Org., Geneva, 1967.

Kuhn, M., L.S. Kundla, and L.A. Stroschein, The radiation budget at Plateau Station, Antarctica, 1966-1967, in *Meteorological Studies at Plateau Station, Antarct. Res. Ser.*, vol. 25, edited by J.A. Businger, pp. 41-73, AGU, Washington, D.C., 1977.

Lang, P.M., L.P. Steele, R.C. Martin, and K.A. Masarie, Atmospheric methane data for the period 1983-1985 from the NOAA/GMCC global cooperative flask sampling network, *NOAA Tech. Memo., ERL CMDL-1*, 1990a.

Lang, P.M., L.P. Steele, and R.C. Martin, Atmospheric methane data for the period 1986-1988 from the NOAA/CMDL global cooperative flask sampling network, *NOAA Tech. Memo., ERL CMDL-2*, 1990b.

Lubin, D., Infrared properties of the maritime Antarctic atmosphere, *J. Clim.*, *7*, 121-140, 1994.

Lubin, D., D. Cutchin, W. Conant, H. Grassl, U. Schmid, and W. Biselli, Spectral longwave emission in the tropics: FTIR measurements at the sea surface and comparison with fast radiation codes, *J. Clim.*, *8*, 286-295, 1995.

Luther, F.M., R.G. Ellingson, Y. Fouquart, S. Fels, N. A. Scott, and W.J. Wiscombe, Intercomparison of Radiation Codes used in Climate Mod-

els (ICRCCM): Longwave clear-sky results: A workshop summary, *Bull. Am. Meteorol. Soc.*, *69*, 40-48, 1988.

Mahesh, A., V.P. Walden, and S.G. Warren, Radiosonde temperature measurements in strong inversions: Correction for thermal lag based on an experiment at South Pole, *J. Atmos. Oceanic. Technol.*, *14*, 45-53, 1997.

McClatchey, R.A., R.W. Fenn, J.E.A. Selby, F.E. Volz, and J.S. Garing, Optical properties of the atmosphere, 3rd ed., *Rep. AFCRL-72-0497*, Air Force Geophys. Lab., Bedford, Mass., 1972.

Moritz, R.E. and D.K. Perovich (Eds.), *Surface heat budget of the arctic ocean science plan, ARCSS/OAII Rep. Number 5*, 64 pp., Univ. of Washington, Seattle, 1996.

Murcray, F.J. and R. Heuberger, Infrared atmospheric absorption and emission measurements, *Antarctic J. U.S., 25(5)*, 244-246, 1990.

Murcray, F.J., and R. Heuberger, Year-round measurement of atmospheric infrared emission at the South Pole, *Antarct. J. U. S.*, *26*(5), 278-281, 1991.

Murcray, F.J. and R. Heuberger, Extended observations of atmospheric infrared absorption and emission, *Antarct. J. U. S.*, *27*(5), 278-279, 1992.

Poole, L.R., and M.C. Pitts, Polar stratospheric cloud climatology based on Stratospheric Aerosol Measurement II observations from 1978 to 1989, *J. Geophys. Res.*, *99*, 13,083-13,089, 1994.

Press, W.H., B.P. Flannery, S.A. Teukolsky, and W.T. Vetterling, *Numerical Recipes: The Art of Scientific Computing*, 2nd ed., Cambridge Univ. Press, New York, 1992.

Randall, W.J., B.A. Boville, J.C. Gille, P.L. Bailey, S.T. Massie, J.B. Kumer, J.L. Mergenthaler, and A.E. Roche, Simulation of stratospheric N_2O in the NCAR CCM2: Comparison with CLAES data and global budget analysis, *J. Atmos. Sci.*, *51*, 2834-2845, 1994.

Reber, C.A, C.E. Trevathan, R.J. McNeal, and M.R. Luther, The Upper Atmosphere Research Satellite (UARS) Mission, *J. Geophys. Res.*, *98*, 10,643-10,647, 1993.

Revercomb, H.E., H. Buijs, H.B. Howell, D.D. LaPorte, W.L. Smith, and L.A. Sromovsky, Radiometric calibration of IR Fourier transform spectrometers: Solution to a problem with the high-resolution interferometer sounder, *Appl. Opt.*, *27*, 3210 - 3218, 1988.

Revercomb, H.E., R.O. Knuteson, W.L. Smith, H.M. Woolf, and H.B. Howell, Spectroscopic inference from HIS measurements of atmospheric thermal emission, in *Optical Remote Sensing of the Atmosphere, Tech. Dig. Ser.*, vol. 4, pp. 590-593, Opt. Soc. of Am., Washington, D. C., 1990.

Rinsland, C.P., R. Zander, J.S. Namkumg, C.B. Farmer, and R.H. Norton, Stratospheric infrared continuum absorption observed by the ATMOS instrument, *J. Geophys. Res.*, *94*, 16,303-16,322, 1989.

Roche, A.E., J.B. Kumer, J.L. Mergenthaler, G.A. Ely, W.G. Uplinger, J.F. Potter, T.C. James, and L.W. Stewart, The cryogenic limb array etalon spectrometer (CLAES) on UARS: Experiment description and performance, *J. Geophys. Res.*, *98*, 10,763-10,775, 1993.

Rothman, L.S., et al., The HITRAN molecular database: Editions 1991 and 1992, *J. Quant. Spectrosc. Radiat. Transfer*, *48*, 469-507, 1992.

Rusin, N.P., *Meteorological and Radiational Regime of Antarctica.*, translated from Russian by the Israel Program for Scientific Translations, U.S. Dep. of Commerce, Washington, D. C., 1964.

Russell, J.M., III, L.L. Gordley, J.A. Park, S.R. Drayson, W.D. Hesketh, R.J. Cicerone, A.F. Tuck, J.E. Frederick, J.E. Harries, and P.J. Crutzen, The Halogen Occulation Experiment, *J. Geophys. Res.*, *98*, 10,777-10,979, 1993.

Schwerdtfeger, W., The climate of the Antarctic, in *World Survey of Climatology*, edited by S. Orvig, vol. 14, pp. 253-355, Elsevier Sci., New York, 1970.

Schwerdtfeger, W., *Weather and Climate of the Antarctic*, Elsevier Sci., New York, 1984.

Smith, W.L., H.M. Woolf, H.B. Howell, H.-L. Huang, and H.E. Revercomb, The simultaneous retrieval of atmospheric temperature and water vapor profiles: Application to measurements with the high resolution interferometer sounder (HIS), in *RSRM '87: Advances in Remote Sensing Retrieval Methods*, edited by H.E. Fleming and J.S. Theon, pp. 189-202, A. Deepak, Hampton, Va., 1989.

Steel, W.H., Interferometers without collimation for Fourier spectroscopy, *Appl. Opt.*, *54*, 151-156, 1964.

Steele, L.P., P.J. Fraser, R.A. Rasmussen, M.A.K. Khalil, T.J. Conway, A.J. Crawford, R.H. Gammon, K.A. Masarie, and K.W. Thoning, The global distribution of methane in the troposphere, *J. Atmos. Chem.*, *5*, 125-171, 1987.

Stokes, G.M., and S.E. Schwartz, The Atmospheric Radiation Measurement (ARM) program: Programmatic background and design of the Cloud and Radiation Test Bed, *Bull. Am. Meteorol. Soc.*, *75*, 1201-1221, 1994.

Stone, R.S., and J.D. Kahl, Variations in boundary layer properties associated with clouds and transient weather disturbances at the south pole during winter, *J. Geophys. Res.*, *96*, 5137-5144, 1991.

Stone, R.S., E.G. Dutton, and J.J. DeLuisi, Surface radiation and temperature variations associated with cloudiness at the South Pole, *Antarct. J. U. S.*, *24*(5), 230-232, 1989.

Thériault, J.-M., P.L. Roney, D. St.-Germain, H.E. Revercomb, R.O. Knuteson, and W.L. Smith, Analysis of the FASCODE model and its H_2O continuum based on long-path atmospheric transmission measurements in the 4.5-11.5-μm region, *Appl. Opt.*, *33*, 323-333, 1994.

Thoning, K.W., P. Tans, T.J. Conway, and L.S. Waterman, NOAA/GMCC calibrations of CO_2-in-air reference gases: 1979-1985, *NOAA Tech. Memo. ERL ARL-150*, Environ. Res. Lab., Boulder, Colo., 1987.

Timofeyev, Y.M., and M.V. Tonkov, Effect of the induced oxygen absorption band on the transformation of radiation in the 6μm region in the Earth's atmosphere, *Izv. Acad. Sci. USSR Atmos. Oceanic Phys.*, Engl. Transl., *14*, 437-441, 1978.

Tzeng, R.Y., D.H. Bromwich, and T.R. Parish, Present-day Antarctic climatology of the NCAR Community Climate Model version 1, *J. Clim.*, *6*, 205-226, 1993.

Tzeng, R.Y., D.H. Bromwich, T.R. Parish, and B. Chen, NCAR CCM2 simulation of the modern Antarctic climate, *J. Geophys. Res.*, *99*, 23,131-23,148, 1994.

Van Allen, R., F.J. Murcray, and X. Liu, Mid-infrared measurements of the atmospheric emission over the South Pole using a radiometrically calibrated Fourier transform spectrometer, *Appl. Opt.*, *35*, 1523-1530, 1996.

Walden, V.P., The downward longwave radiation spectrum over the Antarctic Plateau, Ph.D. thesis, Univ. of Washington, Seattle, 1995.

Walden, V.P., and S.G. Warren, Atmospheric longwave radiation spectrum and near-surface atmospheric temperature profiles at South Pole Station, *Antarct. J. U. S.*, *28*(5), 269-271, 1994.

Walden, V.P., S.G. Warren, F.J. Murcray, and R.G. Ellingson, Infrared radiance spectra for testing radiative transfer models in cold and dry atmospheres: Test cases from the Antarctic Plateau, *Bull. Am. Meteorol. Soc.*, *78*, 2246-2247, 1997.

Warren, S.G., *Antarctica*, in *Encyclopedia of Weather and Climate*, Oxford Univ. Press, New York, 32-39, 1996.

Yamanouchi, T., and S. Kawaguchi, Longwave radiation balance under a strong surface inversion in the katabatic wind zone, Antarctica, *J. Geophys. Res.*, *89*, 11,771-11,778, 1984.

Yamanouchi, T., and S. Kawaguchi, Effects of drifting snow on surface radiation budget in the katabatic wind zone, Antarctica, *Ann. Glaciol.*, *6*, 238-241, 1985.

Yamanouchi, T., M. Wada, S. Mae, S. Kawaguchi, and K. Kusunoki, The radiation budget at Mizuho Station, Antarctica, 1979, *Ann. Glaciol*, *3*, 327-332, 1982.

F. J. Murcray, Department of Physics, University of Denver, 2112 E. Wesley, Denver, CO 80210 (email: murcray@ram.phys.du.edu)

V. P. Walden, Space Science and Engineering Center, University of Wisconsin-Madison, 1225 W. Dayton Street, Madison, WI 53706 (email: von.walden@ssec.wisc.edu)

S. G. Warren, Department of Atmospheric Sciences, University of Washington, Box 351640, Seattle, WA 98195-1640 (email: sgw@atmos.washington.edu)

(Received October 7, 1996; revised April 23, 1997; accepted August 18, 1997.)